BICEP/*Keck* XV: The BICEP3 Cosmic Microwave Background Polarimeter and the First Three-year Data Set

P. A. R. Ade[1], Z. Ahmed[2], M. Amiri[3], D. Barkats[4], R. Basu Thakur[5], C. A. Bischoff[6], D. Beck[2,7], J. J. Bock[5,8], H. Boenish[4], E. Bullock[9], V. Buza[10], J. R. Cheshire IV[9], J. Connors[4], J. Cornelison[4], M. Crumrine[11], A. Cukierman[2,7], E. V. Denison[12], M. Dierickx[4], L. Duband[13], M. Eiben[4], S. Fatigoni[3], J. P. Filippini[14,15], S. Fliescher[11], N. Goeckner-Wald[7], D. C. Goldfinger[4], J. Grayson[7], P. Grimes[4], G. Hall[11], G. Halal[7], M. Halpern[3], E. Hand[6], S. Harrison[4], S. Henderson[2], S. R. Hildebrandt[5,8], G. C. Hilton[12], J. Hubmayr[12], H. Hui[5], K. D. Irwin[2,7,12], J. Kang[5,7], K. S. Karkare[4,10], E. Karpel[7], S. Kefeli[5], S. A. Kernasovskiy[7], J. M. Kovac[4,16], C. L. Kuo[2,7], K. Lau[11], E. M. Leitch[10], A. Lennox[14], K. G. Megerian[8], L. Minutolo[5], L. Moncelsi[5], Y. Nakato[7], T. Namikawa[17], H. T. Nguyen[8], R. O'Brient[5,8], R. W. Ogburn IV[2,7], S. Palladino[6], T. Prouve[13], C. Pryke[9,11], B. Racine[4,18], C. D. Reintsema[12], S. Richter[4], A. Schillaci[5], R. Schwarz[11], B. L. Schmitt[4], C. D. Sheehy[19], A. Soliman[5], T. St. Germaine[4,16], B. Steinbach[5], R. V. Sudiwala[1], G. P. Teply[5], K. L. Thompson[2,7], J. E. Tolan[7], C. Tucker[1], A. D. Turner[8], C. Umiltà[6,14], C. Vergès[4], A. G. Vieregg[10,20], A. Wandui[5], A. C. Weber[8], D. V. Wiebe[3], J. Willmert[11], C. L. Wong[4,16], W. L. K. Wu[2], H. Yang[7], K. W. Yoon[2,7], E. Young[2,7], C. Yu[7], L. Zeng[4], C. Zhang[5], and S. Zhang[5]
(BICEP/*Keck* Collaboration)

[1] School of Physics and Astronomy, Cardiff University, Cardiff, CF24 3AA, UK
[2] Kavli Institute for Particle Astrophysics and Cosmology, SLAC National Accelerator Laboratory, 2575 Sand Hill Rd, Menlo Park, CA 94025, USA
[3] Department of Physics and Astronomy, University of British Columbia, Vancouver, British Columbia, V6T 1Z1, Canada
[4] Center for Astrophysics, Harvard & Smithsonian, Cambridge, MA 02138, USA
[5] Department of Physics, California Institute of Technology, Pasadena, CA 91125, USA; hhui@caltech.edu
[6] Department of Physics, University of Cincinnati, Cincinnati, OH 45221, USA
[7] Department of Physics, Stanford University, Stanford, CA 94305, USA
[8] Jet Propulsion Laboratory, Pasadena, CA 91109, USA
[9] Minnesota Institute for Astrophysics, University of Minnesota, Minneapolis, MN 55455, USA
[10] Kavli Institute for Cosmological Physics, University of Chicago, Chicago, IL 60637, USA
[11] School of Physics and Astronomy, University of Minnesota, Minneapolis, MN 55455, USA
[12] National Institute of Standards and Technology, Boulder, CO 80305, USA
[13] Service des Basses Températures, Commissariat à l'Energie Atomique, F-38054 Grenoble, France
[14] Department of Physics, University of Illinois at Urbana-Champaign, Urbana, IL 61801, USA
[15] Department of Astronomy, University of Illinois at Urbana-Champaign, Urbana, IL 61801, USA
[16] Department of Physics, Harvard University, Cambridge, MA 02138, USA
[17] Kavli Institute for Physics and Mathematics of the Universe (WPI), UTIAS, The University of Tokyo, Kashiwa, Chiba 277-8583, Japan
[18] Aix-Marseille Université, CNRS/IN2P3, CPPM, Marseille, France
[19] Physics Department, Brookhaven National Laboratory, Upton, NY 11973, USA
[20] Department of Physics, Enrico Fermi Institute, University of Chicago, Chicago, IL 60637, USA

Abstract

We report on the design and performance of the BICEP3 instrument and its first three-year data set collected from 2016 to 2018. BICEP3 is a 52 cm aperture refracting telescope designed to observe the polarization of the cosmic microwave background (CMB) on degree angular scales at 95 GHz. It started science observation at the South Pole in 2016 with 2400 antenna-coupled transition-edge sensor bolometers. The receiver first demonstrated new technologies such as large-diameter alumina optics, Zotefoam infrared filters, and flux-activated SQUIDs, allowing $\sim 10\times$ higher optical throughput compared to the *Keck* design. BICEP3 achieved instrument noise equivalent temperatures of 9.2, 6.8, and 7.1 $\mu K_{CMB}\sqrt{s}$ and reached Stokes Q and U map depths of 5.9, 4.4, and 4.4 μK arcmin in 2016, 2017, and 2018, respectively. The combined three-year data set achieved a polarization map depth of 2.8 μK arcmin over an effective area of 585 square degrees, which is the deepest CMB polarization map made to date at 95 GHz.

1. Introduction

Inflation, a brief period of exponential expansion in the early universe, was postulated to solve the horizon, flatness, and monopole problems that arise from the ΛCDM "standard model" of the universe (Brout et al. 1978; Kazanas 1980; Starobinsky 1980; Guth 1981; Albrecht & Steinhardt 1982; Linde 1982). The perturbations under this paradigm are adiabatic, nearly Gaussian, and close to scale-invariant, which are consistent with precise cosmic microwave background (CMB) observations (Planck Collaboration et al. 2020a). Moreover, many models of inflation predict the existence of primordial gravitational waves (PGWs), which would leave a unique degree-scale *B*-mode polarization pattern in the

Table 1
Frequency Coverage in the BICEP/Keck Experiment from 2010 to 2020

Receiver	2010	2011	2012	2013	2014	2015	2016	2017	2018	2019	2020
BICEP2	150 GHz	150 GHz	150 GHz								
Keck Rx0			150 GHz	150 GHz	95 GHz	95 GHz	220 GHz	220 GHz	220 GHz	220 GHz	220 GHz
Keck Rx1			150 GHz	150 GHz	150 GHz	220 GHz	220 GHz	220 GHz	220 GHz	[150 GHz]	
Keck Rx2			150 GHz	150 GHz	95 GHz	95 GHz	220 GHz	220 GHz	220 GHz	220 GHz	220 GHz
Keck Rx3			150 GHz	150 GHz	150 GHz	220 GHz	220 GHz	220 GHz	220 GHz	220 GHz	
Keck Rx4			150 GHz	150 GHz	150 GHz	150 GHz	150 GHz	[270 GHz]	270 GHz	270 GHz	270 GHz
BICEP3						[95 GHz]	95 GHz	95 GHz	95 GHz	95 GHz	95 GHz
BA Rx0											30/40 GHz

Note. Brackets in the table indicate an engineering receiver (270 GHz *Keck* in 2017 was a prototype of high-frequency focal plane, BICEP3 in 2015 only had a partially filled focal plane, and the 150 GHz *Keck* in 2019 was a demonstration of the μMUX readout; Cukierman et al. 2020), and are not included in science analyses. *Keck* was replaced by BICEP ARRAY in 2020. In its first season, one slot was fitted with the 30/40 GHz BICEP ARRAY receiver, and three *Keck* receivers were put back into the new telescope mount. This paper uses the data collected by BICEP3 from 2016 through 2018.

CMB (Kamionkowski et al. 1997; Seljak & Zaldarriaga 1997). If detected, PGWs can serve as a probe of the very early universe and high-energy physics inaccessible with existing particle accelerators.

The BICEP/*Keck* experiments are a series of telescopes designed to search for this degree-scale *B*-mode polarization of the CMB originating from PGWs. These instruments are located at the Amundsen−Scott South Pole Station in Antarctica. The ∼10,000 ft altitude and extreme cold make the Antarctic plateau one of the driest places on Earth. During the winter season, the six months of continuous darkness provides exceptionally low and stable atmospheric $1/f$ noise, which allows our telescopes to observe the sky without the need of an active instrument modulation at these large angular scales (Kuo 2017).

We first reported an excess of *B*-mode signal at 150 GHz in BICEP2 collaboration et al. (2014a). In a subsequent joint analysis with the *Planck* Collaboration, it was found that polarized emission from dust in our galaxy could account for most of the signal (BICEP2/Keck & Planck collaborations et al. 2015). Dust is currently the dominant foreground contaminant to CMB polarization measurements, and is most powerful at high frequencies. Subsequent modeling shows synchrotron may potentially be another source of foreground emission at lower frequencies (Krachmalnicoff et al. 2018). In order to probe the physics of the early universe, we need a dedicated strategy to separate these foregrounds from the potential faint primordial signal.

The BICEP/*Keck* instruments are small-aperture, compact, on-axis refracting telescopes, emphasizing high optical throughput and low optical loading with dedicated calibration campaigns to control instrument systematics. Five separate instruments spanning the past two decades have been deployed to date. BICEP1 operated from 2006 through 2008 with 98 neutron transmutation doped (NTD) germanium thermistors at 95, 150, and 220 GHz (Chiang et al. 2010; Takahashi et al. 2010). BICEP2 replaced BICEP1 and observed from 2010 through 2012 with 512 planar antenna transition-edge sensors at 150 GHz (BICEP2 collaboration et al.2014b). *Keck* utilized the same optical and detector technologies as employed in BICEP2, comprising five independent receivers. It observed at 150 GHz, and later at 95 and 220 GHz, installed in a separate telescope mount previously used for DASI (Leitch et al. 2002) and QUaD (Ade et al. 2008). It began science observations in 2012, observing until 2019 (Kernasovskiy et al. 2012; Staniszewski et al. 2012).

After BICEP2 was decommissioned at the end of 2012, BICEP3 was installed in the same telescope mount in 2014 November and started scientific observation in 2016 with 2400 detectors at 95 GHz. It employed a conceptually similar design to its predecessor, but with multiple technological improvements allowing an order of magnitude increase in mapping speed compared to a single *Keck* 95 GHz receiver. Benefiting from a modular receiver design, *Keck* was gradually adapted from an all 150 GHz receiver configuration into a high-frequency "dust telescope," observing at 220 and 270 GHz, with BICEP3 continuing observations at 95 GHz, where foregrounds are minimal. In late 2019, *Keck* was decommissioned and replaced with a new telescope mount (Crumrine et al. 2018) to accommodate four BICEP3-like receivers that will form the next phase of the experiment, BICEP ARRAY. The first receiver in BICEP ARRAY started observation at 30/40 GHz in 2020 to probe the low-frequency polarized synchrotron signal. BICEP ARRAY will cover six distinct bands from 30 to 270 GHz when fully deployed. In the meantime, the BICEP ARRAY telescope mount carries a mixture of *Keck* and BICEP ARRAY receivers, while BICEP3 continues to observe. Table 1 shows the BICEP/*Keck* experiments from 2010 to 2020 and their frequency coverage.

This paper provides an overview of the BICEP3 instrument design and performance with the three-year data set from 2016 to 2018. Figure 1 shows the overall layout of BICEP3 as it is installed at the South Pole. The following sections describe the details of each of the subcomponents: telescope mount (Section 2); optics (Section 3); cryostat (Section 4); focal plane unit (Section 5); transition-edge sensor bolometers (Section 6); and data acquisition and control system (Section 7).

In particular, BICEP3's 520 mm diameter aperture is ∼2 times the size of the *Keck* design. This is realized by the large-diameter alumina optics shown in Section 3.1. The increase in aperture size allowed us to accommodate 2400 detectors in the focal plane, compared to 288 detectors in the previous *Keck* 95 GHz receivers. The new modular focal plane design in Section 5 allows rapid rework and dramatically reduces risk. The high number of detectors also requires a mature multi-plexing readout. BICEP3 is the first experiment to adapt the new generation flux-activated time domain multiplexing system described in Section 7. Most CMB experiments utilize low temperature, superconducting detectors that operate below 1 K. Rapid development in mechanical compressor cryocoolers allowed ground-based telescopes to phase out the need of liquid helium, but the high-pressure helium lines in the system
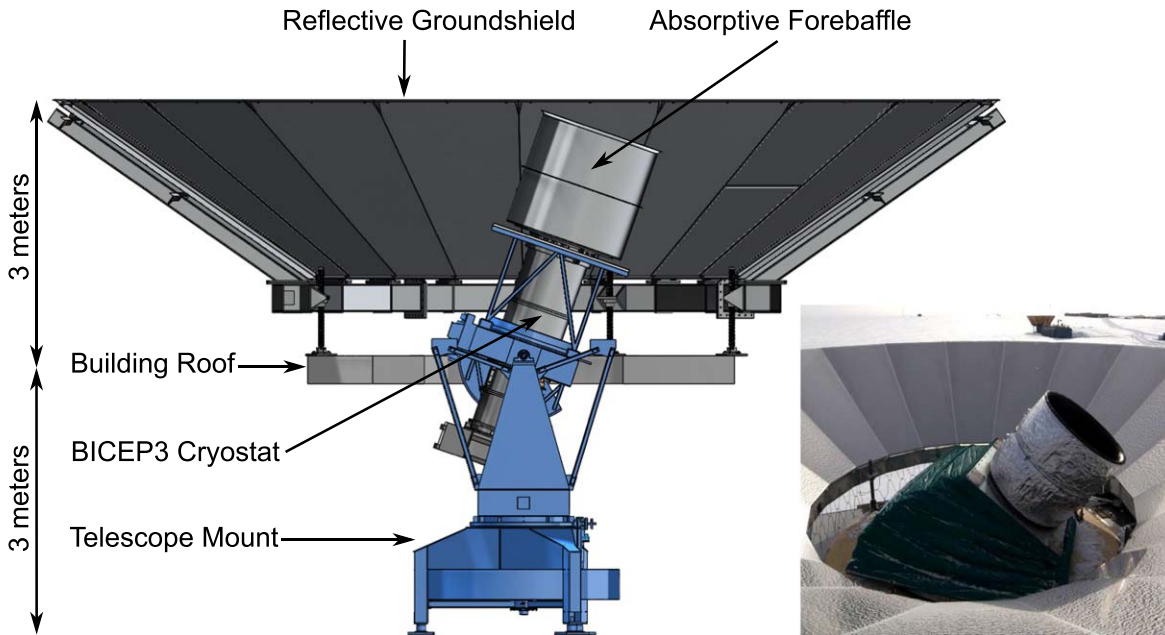
Figure 1. The BICEP3 telescope in the mount, looking out through the roof of the Dark Sector Laboratory (DSL) located ∼1100 m from the geographic South Pole. The insulating environmental shroud shown in the bottom right photo is hidden in the CAD layout. The three-axis mount previously used in BICEP1 and BICEP2 allows for motion in azimuth, elevation, and boresight rotation. A comoving absorptive forebaffle extends skyward beyond the cryostat receiver to intercept stray light outside the designed field of view. Additionally, the telescope is surrounded by a stationary reflective ground shield that redirects off-axis rays to the cold sky.

between the telescope and compressor induce significant wear in a continuous rotating mount. We address this by integrating a helium rotary joint into the telescope mount system, allowing for continuous rotation while maintaining a high-pressure seal and electrical connectivity (Section 2).

The achieved performance characteristics of the receiver and detector properties of BICEP3 are presented in Section 8, the observing strategy is presented in Section 9, and in Section 10 we show the first three-year data set taken from 2016 to 2018, reporting its internal consistency validation, sensitivity, and map depth. The cosmological analysis using *Planck*, Wilkinson Microwave Anisotropy Probe (WMAP), and BICEP/*Keck* observations through the 2018 observing season are presented in BICEP/Keck et al. (2021).

2. Telescope Mount, Forebaffle, and Ground Shield

2.1. Telescope Mount

BICEP3 is installed in the Dark Sector Laboratory building, approximately a kilometer away from the South Pole Station. The base of the telescope mount is supported by a platform on the second floor of the building, with a 2.4 m diameter opening in the roof for telescope access to the sky (Figure 1). The warm indoor environment of the building is extended beyond the roof level by a flexible insulating environmental shield, so that only the receiver window is exposed to the Antarctic ambient temperature.

BICEP3 uses a steel three-axis mount built by Vertex-RSI.[21] It was originally built for BICEP1 and also housed BICEP2 until 2013. The mount structure was modified in 2014 to accommodate the larger BICEP3 receiver.

The mount moves in azimuth and elevation, with the third axis rotating about the boresight of the telescope ("deck" rotation). The range of motion of the mount is 48°–110° in

elevation and 400° in azimuth, capable of scanning at speeds of 5° s^{-1} in azimuth.

The BICEP3 cryostat houses a pulse tube cryocooler that limits the accessible deck angle to less than a full 360° rotation in the BICEP mount. However, the design still allows the telescope to scan with two sets of 180° opposing deck angles, offset from each other by 45°, retaining an effective set of observation schedules in order to probe systematic errors, as shown in Section 9.

2.2. Helium Rotary Joint

The pulse tube cryogenic cooler comprises two subsystems: a coldhead installed inside the receiver, and a helium compressor located in the building, away from the telescope mount. This pulse tube provides cooling by expanding a high-pressure helium gas volume, and requires high and low pressure helium flexible lines to be routed from the compressor, through the three mount axes (azimuth, elevation, and boresight), to the coldhead in the receiver.

During an observing schedule, movements in elevation and boresight are intermittent and span a limited range of angles, unlike the azimuth axis, which scans back and forth continuously in azimuth with a 130° range. To avoid wear on the compressor lines in the helium line wrap, BICEP3 uses a commercial high-pressure gas rotary joint from DSTI[22] that enables the two pressurized helium gas lines to pass through the azimuth motion. In this joint, shown in Figure 2, one set of lines remains static at the base of the mount and connects to the helium rotary joint, from which a second set of lines rotates with the azimuth axis of the mount. Therefore the azimuth cable carrier only needs to handle the much more flexible electrical cables.

During the 2015 engineering season, the original design used a basic two channel rotary joint (DSTI model: GP-421) to

---

[21] Now General Dynamics Satcom Technologies, Newton, NC 28658, http://www.gdsatcom.com/vertexrsi.php.

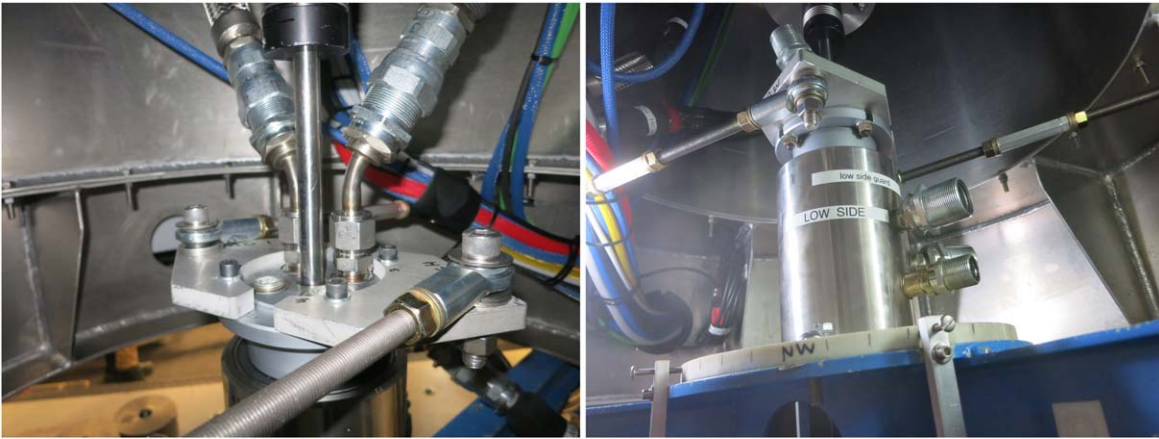[22] Dynamic Sealing Technologies, Inc., Andover, MN 55304, www.dsti.com.

Figure 2. Photos of the four channel helium rotary joint (HRJ) system. Left: two 30° bends rotate with the azimuth axis and go on to the receiver through the elevation and boresight axes. Right: static section with the four connections for the high and low pressure helium and their respective guard channels. In both photos, two ball-end rod joints act as torque arms to transmit the azimuth rotation to the rotor of the HRJ.

connect the compressor's high and low pressure helium channels at 290 and 90 PSI, respectively. However, helium gas can permeate materials and gaps much more easily than other larger gas molecules, and this commercial rotary joint was not designed specifically for helium gas. We found the overall system lost 3–5 PSI of pressure per day, originating in the dynamic seals of the rotary joint. Such a large leak resulted in the need to refill the compressor system multiple times a week to maintain optimal pulse tube performance. In addition to being extremely labor intensive for the telescope operator, these repeated helium refills introduced contamination into the pulse tube, and eventually degraded the cooling performance.

To remedy the high leak rate, the rotary joint was replaced with a four channel model (DSTI model: GP-441) before the 2016 season. The four channels were configured such that the two working high-pressure helium lines would be guarded by two outer channels, serving as pressurized buffers. Thus, the dynamic seals between the two inner high-pressure lines would only "sense" the small differential pressure to the pressurized buffers (∼10 PSI) instead of the much larger differential to atmospheric pressure (>100 PSI). This configuration reduced the leak rate of the active channels to between ∼0.1 and 0.5 PSI per day over an entire season.[23] The reduced helium leak rate requires less frequent refills, and enables optimal pulse tube performance throughout a full season. The HRJ dynamic seals receive a complete replacement once per year.

2.3. Ground Shield and Absorptive Baffle

A warm, absorptive forebaffle as shown in Figure 1 extends skyward beyond the cryostat receiver to intercept stray light outside the designed field of view. The forebaffle is mounted directly to the receiver and therefore comoving with the axes of motion of the telescope. The forebaffle is constructed from a large aluminum cylinder, 1.3 m in diameter and height, with a rolled top edge lined by microwave-absorptive Eccosorb HR-10 foam. Heater tape keeps the forebaffle a few degrees above the Antarctic ambient temperature to help avoid snow accumulation, and a layer of closed-cell polyethylene foam (Volara) protects the Eccosorb from accumulating moisture. Based on radiative loading on the detectors observed once the

forebaffle is installed, the forebaffle contributes ∼10% of the total optical power. The source of this wide-angle response is likely a combination of scattering and multiple reflections.

Additionally, the telescope is surrounded by a stationary reflective ground shield. It is fixed to the roof of the building to act as a second barrier against stray light and signal contamination from nearby ground sources and reduces the large radiative gradient between the sky and the ground. The ground shield is 10 m in diameter and 3 m in height, constructed with aluminum honeycomb panels and steel beams. The combination of the baffle and the ground shield is designed such that off-axis rays from the telescope must diffract at least twice before intercepting the ground.

2.4. Star Camera

An optical camera is used to determine mount pointing parameters (Section 9.4). It is attached to the side of the receiver vacuum jacket, and looks up through a hole in the bottom of the forebaffle. An optical baffle reduces stray light when using the star camera during daylight and twilight conditions, but is removed for CMB observations. The telescope is a Newtonian reflector, with a 10 cm aluminum-coated[24] objective and a 44 cm focal length. A 700 nm low-pass edge filter removes much of the Rayleigh-scattered sunlight during daylight and twilight. The camera is a CCD with video readout,[25] and the video-to-digital conversion is done with a video capture card[26] in one of the control computers. The field of view is approximately $0.8° \times 0.6°$. The CCD is on a linear stage to allow focusing via a remote controller used by the operator.

3. Optics

3.1. Optical Design

BICEP3 utilizes the same concept as previous BICEP/*Keck* receivers, using a compact, on-axis, two-refractor optical design that provides a wide field of view and a telecentric

---

[23] The guard channels still have similar leak rate as the two channel design, but this is acceptable since refills for them do not affect the pulse tube performance.

[24] Edmund Optics, Inc., Barrington, NJ, USA.
[25] Astrovid StellaCam Ex, Adirondack Video Astronomy, 72 Harrison Ave., Hudson Falls, New York, USA; the CCD is a Sony ICX248AL B/W, Sony Group Corporation, 1-7-1 Konan Minato-ku, Tokyo, 108-0075 Japan.
[26] Sensoray, 7313 SW Tech Center Dr., Tigard, OR, USA.

Table 2
Optical Design Parameters for BICEP2 at 150 GHz and BICEP3 at 95 GHz

	BICEP2/ Keck	BICEP3
Aperture dia.	264 mm	520 mm
Field of view	15°	27.4°
Beamwidth σ	12′	8′.9
Focal ratio	$f/2.2$	$f/1.6$

focal plane. It has a 4 K aperture of 520 mm and beamwidth given by a Gaussian radius $\sigma \sim 8.9′$. The lenses and filters operate at cryogenic temperatures inside of the cryostat receiver to minimize excess in-band photon loading. The HDPE plastic cryostat window is at ambient temperature. Thermal filters mounted behind the window cool radiatively. Table 2 shows BICEP3's optical design parameters compared to previous BICEP/*Keck* receivers.

The ray diagram and full optical chain are shown in Figure 3. The radially symmetric optical design allows for well-matched beams for two idealized orthogonally polarized detectors at the focal plane.

3.2. Vacuum Window and Membrane

The first optical element in the receiver is the vacuum window. BICEP2/*Keck* used laminated Zotefoam[27] (Zotefoam HD30), but BICEP3 instead uses a 31.75 mm thick, 73 cm diameter high-density polyethylene (HDPE) window due to the larger aperture setting more stringent requirements on its mechanical strength. The surfaces of the HDPE window are coated with a $\lambda/4$ antireflective (AR) layer made of Teadit 24RGD[28] (expanded PTFE sheet). The AR coating adheres to the window with a thin layer of low-density polyethylene plastic, melted in a vacuum oven press.

In front of the window is a 22.9 μm thick biaxially oriented polypropylene membrane to protect the window from snow and create an enclosed space below, which is slightly pressurized with room-temperature nitrogen gas to evaporate snow that falls onto the membrane surface.

3.3. Large-diameter 300 K Filters

Inside the receiver and directly behind the vacuum window is a set of infrared filters to reduce the thermal loading in the receiver. These are a stack of 10 thin filters mounted on a set of aluminum rings mechanically connected to the room-temperature vacuum jacket. The filters reflect or absorb infrared radiation in stages, and radiatively equilibrate at progressively lower temperatures to reduce the thermal infrared power into the cryostat.

The original design used a set of metal-mesh filters, composed of 3.5 μm Mylar or 6 μm polypropylene/polyethylene (PP/PE) film, prealuminized to a 40 nm deposition thickness and laser ablated to form a grid of metal squares (Ahmed et al. 2014). However, we found that the performance of the metal-mesh filter depended on the etching process of the metal on the thin film, and minor defects in fabrication introduced excess in-band scattering from the filters. The in-
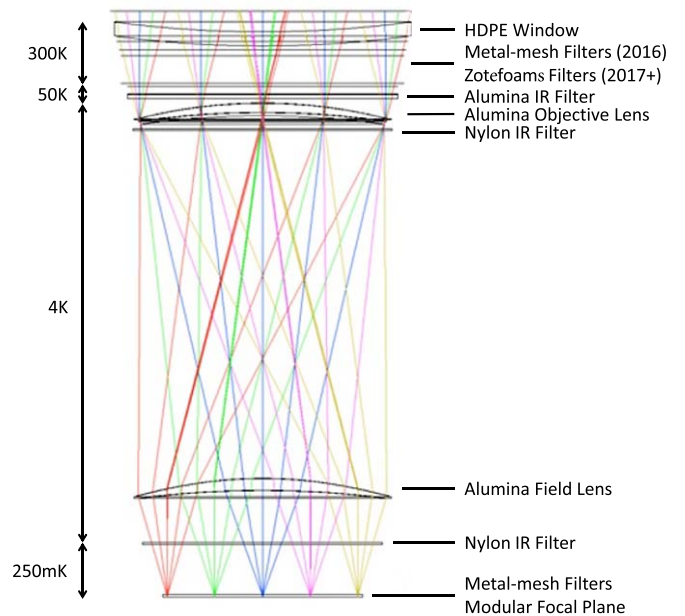

Figure 3. Ray diagram including the elements of the optical chain. The 300 K metal-mesh filters were replaced by a stack of 10 Zotefoam filters in 2017, which improved both the IR loading on the cryostat and the in-band power incident on the detectors.

band scattering was slightly polarized, leading to additional millimeter-wave power on the detectors and associated photon noise. Furthermore, simulations using high-frequency structure simulator (HFSS[29]) software indicated of order 0.5% specular reflection per layer even without defects.

All of the metal-mesh filters except for one placed behind the 50 K alumina filter were replaced in 2017 with a set of ten 3.17 mm thick Zotefoam layers (Figure 4). These filters are nitrogen-expanded polyethylene foam layers that both scatter and absorb/emit infrared radiation (IR) isotropically and therefore act as floating blocking layers (Choi et al. 2013), while maintaining >99% transmission in-band. Using room-temperature transmission measurements, we estimate an 8% improvement of in-band transmission compared to the metal-mesh filters. Table 3 details the individual filters used in BICEP3.

3.4. Alumina Thermal Filter and Optics

Motivated by the larger aperture diameter and faster $f/1.6$ speed in BICEP3, we developed large-diameter alumina filters and their antireflection coating. Alumina lenses are much thinner and less aggressively shaped than their HDPE equivalents owing to the significantly higher index of refraction at $n = 3.1$. The alumina optics are 21 and 27 mm thick at the center for the field and objective lens, respectively, compared to >67 mm for a comparable HDPE design. Both the lenses and 50 K filter are made from 99.6% pure alumina sourced from CoorsTek.[30]

The reduction in thickness and high thermal conductivity of alumina (0.5 W m^{-1} K^{-1} at 4 K) enables the optical elements to cool to base temperatures more rapidly and limits any thermal gradient across the lenses to less than 1 K from center to edge. Lab measurements of similar alumina materials indicate low in-
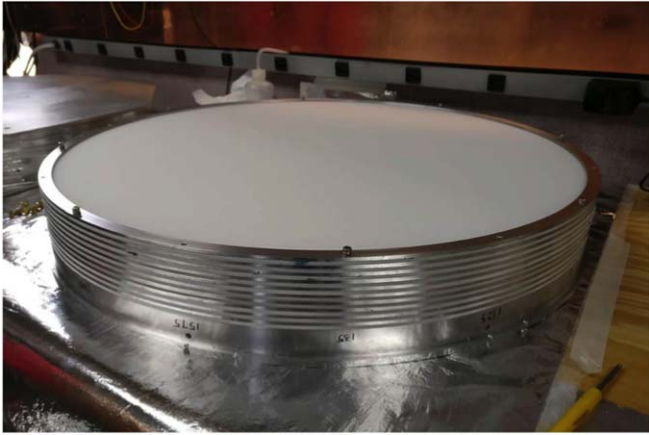
Figure 4. Stack of 10 layers of room-temperature IR filters installed in BICEP3, immediately behind the vacuum window. This photo shows the current configuration, with each layer composed of 3.17 mm thick HD30 foam, glued onto a stack of aluminum frames with 3.17 mm spacing. The original design was a stack of metal-mesh filters, which was replaced in 2017.
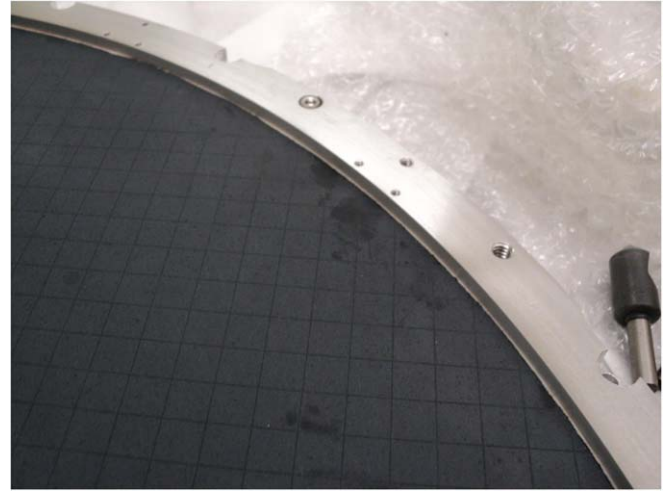
Table 3
Room-temperature IR Filters Installed in BICEP3

Location	2016 Substrate	Square/pitch (μm)	2017+ Substrate
Behind window ($\sim$290 K)	3.5 μm Mylar	50/80	HD30 foam
	3.5 μm Mylar	40/55	HD30 foam
	3.5 μm Mylar	50/80	HD30 foam
	3.5 μm Mylar	40/55	HD30 foam
	3.5 μm Mylar	90/150	HD30 foam
	6 μm PP/PE	40/55	HD30 foam
	3.5 μm Mylar	50/80	HD30 foam
	3.5 μm Mylar	40/55	HD30 foam
	3.5 μm Mylar	50/80	HD30 foam
	3.5 μm Mylar	90/150	HD30 foam
Behind 50 K Alumina filter	3.5 μm Mylar	90/150	3.5 μm Mylar

Note. The main stack of 10 filters behind the window are listed in order beginning with the closest filter to the window. The metal-mesh filters were replaced by Zotefoam in 2017.

band absorption at room temperature that decreases with temperature (Penn et al. 1997; Inoue et al. 2014). Our own measurements at room temperature indicated significant differences between various formulae, and the CoorsTek AD-996 Si used for the filter and lenses was the best we tested. After deployment, we also confirmed a substantially decreased loss at 77 K. A single 10 mm thick alumina disk serves as an absorptive thermal filter, mounted on the 50 K cryogenic stage. The high mid-infrared absorption and high thermal conductivity make alumina a choice material for this application.

The AR coating used for the alumina optics is a mixture of Stycast 1090 and 2850FT with a homogeneous refractive index of $n = 1.74$. The epoxy is poured and rough molded to 1 mm thickness on the alumina surface, then either machined (lenses) or abrasively ground (flat filter) to the final 0.452 mm thickness. The thickness of the coating is controlled to less than 25 μm tolerance by referencing precoating surface measurements of the alumina.

Historically, alumina optics were limited to small sizes unless accommodation for differential contraction between the alumina and the epoxy was made. Inoue et al. (2014) and

Figure 5. AR coated alumina filter in BICEP3. The alumina filter is coated with a mix of Stycast 1090 and 2850FT. The epoxy is machined to the correct thickness and laser diced to 1 cm squares to mitigate differential thermal contraction between alumina and the epoxy.

Rosen et al. (2013) put slices through their coatings to allow cryogenic operation. We adopted a laser-cutting technique using Laserod,[31] the same commercial laser machining company that etched the IR blocking metal-mesh film filters described above. The laser cuts in the AR epoxy are $\sim$30 μm wide, tuned to reach the alumina surface, and spaced every 10 mm in a square grid pattern (Figure 5).

3.5. Nylon IR Blocking Filters

Following the same machining and coating approach in BICEP2/*Keck* (BICEP2 collaboration et al. 2014b), two Nylon IR blocking filters are placed in the receiver. One is behind the aperture stop, and the other is behind the field lens, above the focal plane (FPU) assembly, both at 4 K. Nylon strongly absorbs far-infrared radiation (Halpern et al. 1986) and thus reduces radiated power from 50 K from reaching the 280 mK focal plane.

3.6. Metal-mesh Low-pass Edge Filters

A set of metal-mesh low-pass edge filters (Ade et al. 2006) with a cutoff at 4 cm^{-1} were used to control any out-of-band response in the detectors. They are made from multiple polypropylene substrate layers, each coated with copper grids in different sizes, and hot-pressed together to form a resonant filter.

Prior to the 2017 season, these filters were cut into 76×76 mm squares and independently mounted onto each detector module (Section 5) at 280 mK. We found anomalous detector spectral responses in the 2016 FTS measurements described in Section 8.1. Upon examining the filters at the end of the 2016 season, we found the layers had delaminated. It was determined that the cause of delamination was likely insufficient oven temperature during fabrication. Furthermore, the cutting of individual, smaller filters introduced extra stress on the edge contributing to the delamination.

New filters were fabricated using a higher oven temperature in the fusing process. The filter design was modified to a larger $\sim$23 $\times$15 cm size covering five detector modules. This change

---

[31] Laserod Technologies LLC, Torrance, CA 90501, USA.

reduced mechanical stress at the filter edges caused by the dicing process. Extra spring loaded washers and widened mounting slots allowed the filter to slide more freely during thermal contraction. These modifications were done at the end of the 2016 season and subsequent FTS measurements showed no evidence of filter delamination.

3.7. Optical Loading Reduction

The dominant noise source in BICEP3 is the photon noise of the in-band power. For better sensitivity, it is important to minimize the internal non-sky instrument load.

We measured the upper limit of the total internal loading by measuring the detector load curves with a flat aluminum sheet mounted just beyond the cryostat window. The detector beams in the middle of the focal plane were reflected back into the cryostat and trace all the way back to the sub-Kelvin focal plane, passing through the optical chain twice. The general detector load curve measurements are described in Section 8.2. The detector beams were reflected and therefore received power only from within the cryostat. The comoving forebaffle loading is measured by differencing of the detector response with and without the forebaffle during clear weather while looking at zenith.

The optical power coupled to the detectors due to each individual optical element is calculated by using the transmission properties of the material and finding the source temperature distribution. The calculation incorporates the cumulative optical efficiency from the detector up to the source, and includes the emissivity of the source itself. For the 2016 design, a simple scattering model is used for the room-temperature metal-mesh filters, in which each filter isotropically scatters a small fraction of the radiation to wide angles and warm surfaces around them. Table 4 shows the modeled in-band loading estimate for each of the individual elements and the total measured loading. The agreement between them validates the model assumption.

A significant contributor to the cryostat internal loading was the scattering of the metal-mesh IR-reflective filters before their replacement in 2017 with the Zotefoam filters. The reduction of scattered radiation coupling to the filters and telescope forebaffle results in a decrease of the total instrument loading by 30%.

Non-sky loading also comes from the room-temperature HDPE cryostat window, which now dominates the internal power. We are developing thinner materials that can potentially replace the window in future seasons (Barkats et al. 2018).

4. Cryostat Receiver

4.1. Overview

The cryostat receiver is a compact, cylindrical design that allows for a large optical path while maintaining sub-Kelvin focal plane temperatures (Figure 6). The fully populated receiver weighs about 540 kg without the attached electronics subsystems. The outermost aluminum vacuum jacket is 2.4 m tall along the optical axis and 73 cm in diameter, excluding the pulse tube cryocooler extension. It maintains high vacuum for thermal isolation and is capped at one end by the HDPE plastic window, as described in Section 3.1.

The wide-field refractor design allows for ground-based characterization in the optical far field. The optical design further allows the use of a comoving, absorptive forebaffle (Section 2.3) that terminates wide-angle responses from the

Table 4
Per-detector In-band Optical Load

Source	Load (pW)	T_{RJ} (K)
4K lenses and elements	0.15	1.0
50K alumina filter	0.12	0.9
Metal-mesh filters (2016)	0.63	5.2
HD30 foam filters (2017+)	0.10	0.8
Window	0.69	5.9
Total cryostat internal (2016)	**1.60**	**13.0**
Total cryostat internal (2017+)	**1.10**	**8.6**
Forebaffle (2016)	**0.31**	**2.7**
Forebaffle (2017+)	**0.14**	**1.1**
Atmosphere	1.10	9.9
CMB	0.12	1.1
Total (2016)	**3.13**	**27**
Total (2017+)	**2.46**	**21**

Note. The total loadings listed in **bold** are direct measurements from detector load curves, which are in good agreement with the individual modeled optical elements. A stack of 300 K metal-mesh filters used in the 2016 season were replaced by HD30 foam filters for the 2017 season.

receiver. Cooling most of the optical elements, including the internal baffling between the lenses, to less than 4 K reduces the thermal photon noise seen by the detectors, maximizing the sensitivity of the instrument.

4.2. Cryogenic and Thermal Architecture

Nested within the room-temperature vacuum jacket are the 50 and 4 K stages, each composed of cylindrical aluminum radiation shields and cooled by the first and second stages of the PT-415 pulse tube cryocooler,[32] which provides continuous cooling to 35 K at the "50 K stage" under typical 26 W load and 3.3 K at "4 K stage" under 0.5 W load. The stages are mechanically supported off each other and the vacuum jacket by low thermal conductivity G-10 fiberglass. Multilayer insulation (MLI) wrapped around radiation shields minimizes radiative heat transfer between the 300−50−4 K stages.

A non-continuous, three-stage (^{4}He/^{3}He/^{3}He) helium sorption fridge from Chase Research Cryogenic[33] is heat sunk to the 4 K stage and cools the sub-Kelvin focal plane and supporting structures. The focal plane and ultra-cold (UC 250 mK) stage is a planar copper assembly mounted in a vertical stack on two buffer stages, the intercooler ^{3}He (IC 350 mK) and ^{4}He (2K) stages, each supported and isolated by carbon fiber trusses (Figure 7). The UC stage cools a 9 mm thick, 46 cm diameter focal plane plate that supports the detector modules and a thinner secondary plate. These plates are made from gold-plated, oxygen-free high thermal conductivity copper. The secondary plate and the focal plane are separated by seven 5 cm tall stainless steel blocks that serve as passive low-pass thermal filters to dampen thermal fluctuations to the focal plane. The focal plane and the UC stage are actively temperature controlled in a feedback loop to 274 mK and 269 mK, respectively, using neutron transmutation doped (NTD) germanium thermometers and a resistive heater. Thermal fluctuations on the focal plane during CMB observation are controlled to <0.1 mK.
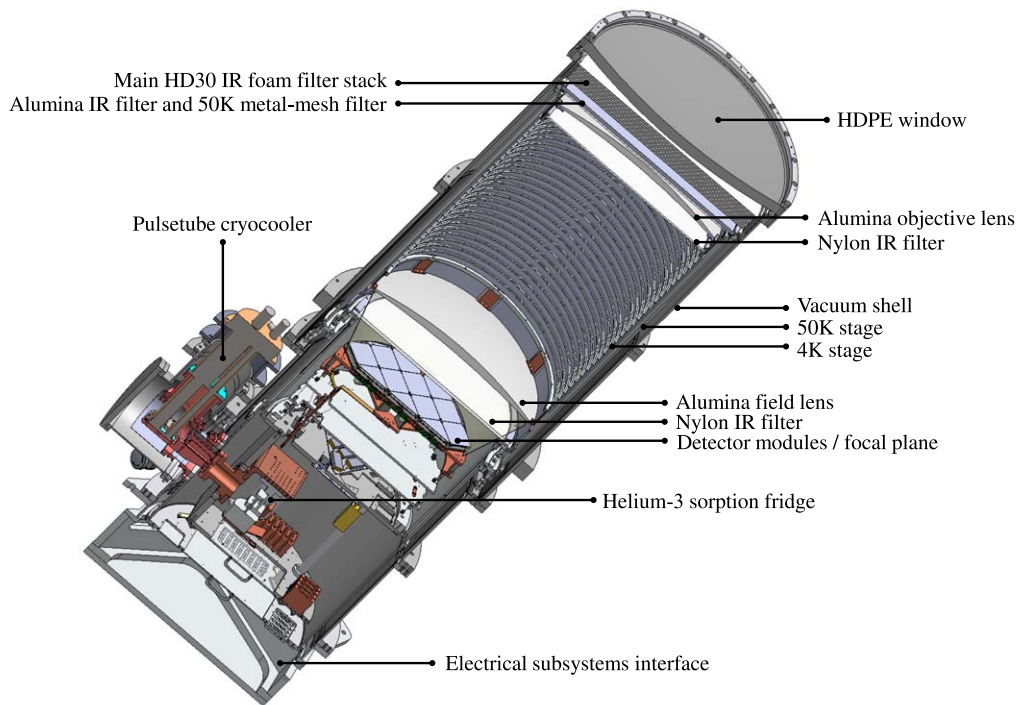
Figure 6. Cutaway view of the BICEP3 cryogenic receiver. The thermal architecture is separated into a two-stage pulse tube cryocooler (50 K, 4 K stages) and a three-stage helium sorption fridge (2 K, 350 mK, 250 mK stages). All thermal stages are mechanically supported by sets of carbon fiber and G-10 fiberglass supports. The focal plane, with 20 detector modules and 2400 detectors, is located at the 250 mK stage, surrounded by multiple layers of RF and magnetic shielding.
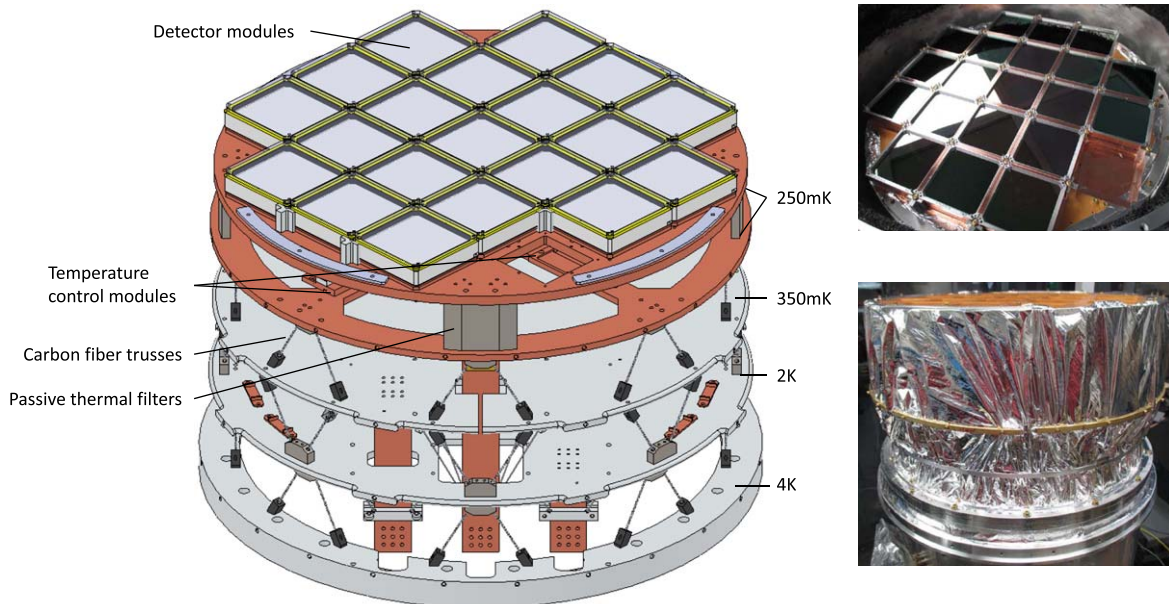

Figure 7. Left: exploded view of the BICEP3 sub-Kelvin stages. Each temperature stage is mechanically supported by sets of carbon fiber trusses. Sets of stainless steel supports connect the two 250 mK copper plates, passively low-pass filtering thermal fluctuations, and two active temperature control modules maintain thermal stability over observation cycles. Right, top: the assembled focal plane with 20 detector modules installed into the 250 mK stage without metal-mesh edge filters. The module slot in the lower right is empty due to the capacity of the readout electronics. Right, bottom: a thin aluminized Mylar shroud extends from the top of the focal plane assembly to the bottom of the 4 K plate to close the 4 K Faraday cage.

4.3. Thermal Performance

The sum of all incident thermal power on the 50 and 4 K stages determines the temperature profile of the elements along each stage and the base operating temperature of the pulse tube.

The room-temperature HDPE plastic window emits ~110 W of power into the receiver while the pulse tube cryocooler is rated for less than 40 W on the 50 K stage. We employed two different types of thermal filters at 300 K mounted just behind the cryostat window to reject the majority of the IR load: (1) a stack of thin film, IR-reflective, capacitive metal-mesh filters in 2016; and (2) a stack of Zotefoam filters starting in 2017. The reason for switching the design is discussed in Section 3.3.

Stages	2016 Temp/Load	2017+ Temp/Load
50 K tube top	58 K	53 K
50 K tube bottom	52 K	49 K
50 K tube loading	19 W	13 W
4 K tube top	4.96 K	4.68 K
4 K tube bottom	4.58 K	4.33 K
4 K tube loading	0.18 W	0.15 W
350 mK stage	354 mK	352 mK
350 mK loading	91 μW	84 μW
250 mK stage	245 mK	244 mK
250 mK loading	3.50 μW	3.35 μW
Focal Plane	268 mK	268 mK

An alumina filter is heatsunk to the 50 K stage to provide absorptive IR filtering due to Alumina's mid-infrared absorption and high thermal conductivity. This replaced the filters used in previous telescopes. Two additional nylon filters are placed in the 4 K stage of the receiver to reduce thermal loading on the sub-Kelvin focal plane by absorbing infrared radiation. Table 5 shows the final temperature and power deposited onto each cryogenic stage. Switching from metal-mesh filters to Zotefoam filters in 2017 reduced the thermal loading and improved the cryogenic hold time of the sub-Kelvin fridge from ∼50 to >80 hr, with 6 hr of recycling time due to improvement of the 4 K base temperature, allowing closer to full condensation of ³He in the sub-Kelvin fridge. This permits the continuous three-day observation schedule shown in Section 9.2.

4.4. Cryogenic Thermal Monitoring and Control

For general thermometry down to 4 K, we use silicon diode thermometers (Lakeshore[34] DT-670), with thin-film resistance temperature detectors (Lakeshore Cernox RTDs) on the sub-Kelvin stages. NTD germanium thermometers are integrated in the secondary UC stage, copper focal plane, and each detector module for more sensitive measurements of the temperatures. The NTDs on the secondary UC stage and focal plane are packaged with a heater to provide active temperature control on their respective temperature stages.

Thermal operations are controlled by a custom-built system similar to the one used in BICEP2/*Keck*. It contains electronic cards used to bias and read out thermometers, control heaters, and provide temperature control servos, and is mounted directly to the cryostat vacuum jacket and interfaces with MicroD (MDM) connectors[35] at the cryostat. Signals from the system are routed to the rack-mounted BLASTbus analog-to-digital converter (ADC) system (Wiebe 2008) next to the telescope that generates the AC bias used for the resistive thermometers and the NTDs, and demodulates the thermometer signals, which are then digitized at ∼100 Hz.

4.5. Radio Frequency Shielding

Several levels of radio frequency (RF) shielding are designed into the 4 K stage and sub-Kelvin structures to minimize RF coupling to the detectors. All cabling inside the cryostat uses twisted pairs, except for the short lengths of flex ribbon cable connecting the detector modules to the focal plane readout circuit board. These ribbon cables are shielded by the detector module, copper focal plane module cutout, and the ground plane of the circuit board that accepts the cable. The 4 K nonoptics volume is designed as a Faraday enclosure, with all seams taped with conductive aluminum tape and cabling passing through inductive-capacitive PI-filtered connectors.[36] The cage is continued to enclose the stack of sub-Kelvin stages by wrapping and sealing a single layer of aluminized Mylar between the 4 K stage and the edge of the focal plane. The niobium enclosure of each detector module and detector tile ground plane close the sky side of the Faraday cage. Upon exiting the cryostat, all of the detector signal lines immediately interface with a capacitive filtered connection on the readout electronics box that is directly mounted on the cryostat.

During the 2015 engineering season, we found an azimuth-synchronous signal strongly affecting the detectors, largely common-mode across a large fraction of detectors within each readout system. This interference showed variation 1000 times larger than the 50 μK CMB temperature variations, causing "SQUID jumps" because of the strong signals. Our detector readout scheme works through feedback to maintain linearity in the SQUID amplification curve (Section 7.1), but large current variations can disrupt the feedback and cause the readout to jump to a different part of the SQUID curve. We discovered that this interference signal was caused by RF emission from the South Pole Station land mobile radio (LMR) system at 450 MHz, coupling into the cryostat and detectors through the cryostat window. BICEP3 is inherently more susceptible to this 450 MHz signal than *Keck* due to its larger aperture, which has a cutoff frequency at 340 MHz at the optics cylinder.

Prior to the 2016 season, we applied silver loaded paste between the detector modules and copper focal plane, so that reliable electrical conductivity was maintained from the modules to the focal plane. In 2015, only 9 out of 20 detector modules were filled, leaving large gaps at the top of the focal plane. In 2016, having the full population of 20 detector modules provided a better RF shielded enclosure. After implementing the improved internal cryostat shielding, RF susceptibility in the range of 400–500 MHz was reduced by 10 dB. In addition, the LMR antenna was changed to a directional sector antenna with reduced power output toward the telescope. Attenuators were also installed to reduce the overall broadcast power, which was tested to be much more powerful than necessary to maintain radio communication across the base. In total, the LMR source power seen at the telescope was reduced by 35 dB. Azimuth scanning tests conducted after these changes have shown none of the visible structure seen in 2015.

4.6. Magnetic Shielding

Earth's magnetic field (∼50 μT) is the most dominant magnetic environment. While this azimuth-fixed signal is largely filtered out during analysis, instrumental magnetic

[34] Lake Shore Cryotronics, Westerville, OH 43082, USA, www.lakeshore.com.
[35] Glenair Inc., Glendale, CA 91201, USA, www.glenair.com.
[36] Cristek Inc., Anaheim, CA 92807, USA, www.cristek.com.

shielding is crucial to minimize coupling to the TES detectors and the SQUID amplifiers. We incorporate two methods of shielding in the cryostat. First we use a cylindrical, high-permeability Amumetal-4K (A4K)[37] structure, with open ends to avoid interference with the optics and allow data cabling through the bottom. It is a split shield on the inner surface of the vacuum jacket of the cryostat. The two halves overlap midway, near the focal plane level given the constraints of the cryostat and optics. Additionally, a shorter, superconducting niobium cylinder is mounted on the 4 K stage, surrounding the focal plane. Lab tests showed a shielding factor of ~ 30 for the magnetic field amplitude along the cylindrical axis of the cryostat.

The detector module, which includes layers of niobium, aluminum, and high-μ A4K (Section 5.1), provides further shielding of the first-stage SQUID amplifier chips on the sub-Kelvin focal plane. The series SQUID array (SSA) on the 4 K stage are packaged in niobium boxes and additionally wrapped with 10 layers of high-μ Metglas 2714A.[38] Overall, BICEP3 shows an induced response ~ 7 $\mu K_{CMB} \mu T^{-1}$, or $350 \mu K_{CMB}/B_{Earth}$ by directly measuring the SQUID amplifier response to a Helmholtz coil.

Another method to estimate impact of the external magnetic field on the data is using the dark SQUID channels in the readout system (Section 7.1). These channels are connected to the SQUID amplifiers, but not the detectors, hence ideally they only respond to external magnetic fields as the telescope scans. Lab measurements show the properties and calibrations of these dark SQUID channels are similar to the other SQUID channels in the same SQUID chip. Then using the neighboring optical channel calibrations and telescope pointing, we constructed "maps" of these dark SQUIDs. Comparing these maps and the associated spectrum with single optical channel maps, we found the dark SQUID responses are factor of 2–20 smaller than the Q/U noise of the same bins (Figure 8).

5. Focal Plane

BICEP3 has 2400 detectors, a factor of nine greater than a single *Keck* receiver at the same frequency. The detectors are fabricated on 20 silicon wafers, each consisting of 60 dual-polarized detector pairs. Each wafer is packaged into a focal plane module with its cold readout electronics and installed onto the copper focal plane to form the BICEP3 focal plane (Figure 9). The focal plane base plate provides the necessary thermal stability, magnetic shielding, and mechanical alignment to operate the detectors. The modular design allows individual detector tiles to be replaced with minimum impact to the rest of the receiver.

5.1. Modular Packaging

Each detector module is $79 \times 79 \times 22$ mm in size (Figure 10). Two 60 pin, 0.5 mm pitch flex ribbon cables connect between each module and the focal plane circuit board, via a pair of zero-insertion force (ZIF) surface-mount connectors. The module mounts on the focal plane on all four corners.

The detector module consists of a quartz antireflection coating, detector tile, niobium (Nb) $\lambda/4$ backshort, A4K magnetic shield, and alumina and PCB readout circuit boards.
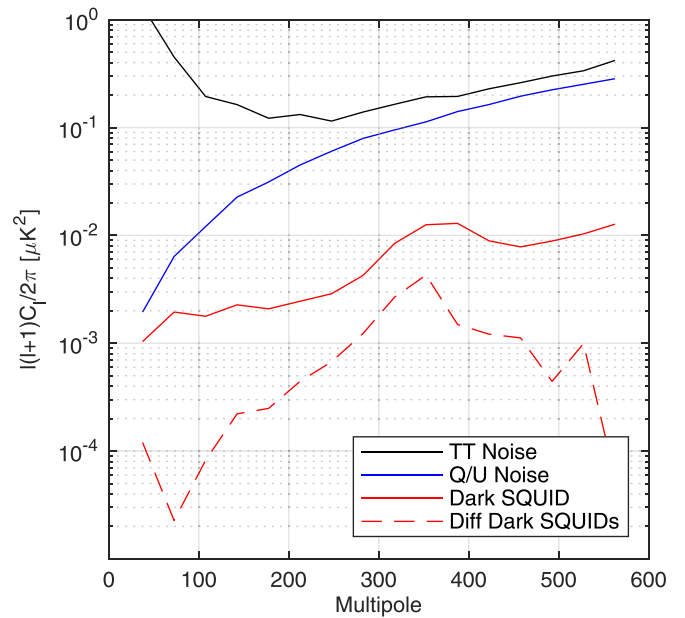

Figure 8. Temperature (black) and polarization (blue) noise of BICEP3. The dark squids (red) is a readout channel that is disconnected from the detector, but sensitive to an external magnetic field. This can be compare to the temperature (black) noise of BICEP3. The dashed red line shows the data by pair-differencing two dark squid channels, which can be compared to the polarization (blue) noise. This comparison demonstrates the magnetic pickup in science data is subdominant.

These subcomponents are stacked together on the aluminum detector frame, secured at the corners with commercially available copper clips,[39] and aligned with 2 mm diameter copper pin-slot pairs located on opposing edges of the wafer. The module is enclosed with a niobium housing, an external niobium magnetic shield covering the ribbon cables, and a copper heatsink.

The readout circuit boards are composed of an alumina and an FR4 printed circuit board. The 0.25 mm thick alumina circuit board has 0.13 mm wide, 0.23 mm pitch aluminum traces, creating a superconducting path between the detectors and the SQUID chips. Twelve readout SQUID and Nyquist chips are mounted onto individual alumina carriers that are glued onto the alumina circuit board. On top of the alumina board is a two-layer FR4 circuit board with standard copper traces. These components are electrically connected to each other with aluminum wire bonds, and two 60 pins surface-mount connectors are soldered on top of the FR4 circuit board for the flex cables shown in Figure 11.

5.2. Thermal Sinking and Magnetic Shielding

The detector tiles are thermally sunk to the aluminum frame on all four sides with ~ 500 0.5 mm pitch gold wirebonds. Additionally, these wirebonds form the top RF shield of the system by connecting the aluminum frame and detector Nb ground plane.

The detector module is mounted to a copper heatsink at the back of the niobium housing. It is supported by three thermally isolated alumina spacers in the corners, making the centermost point the only point of thermal contact between the copper and niobium. This single contact point cools the module housing from the middle, ensuring that the niobium superconducting
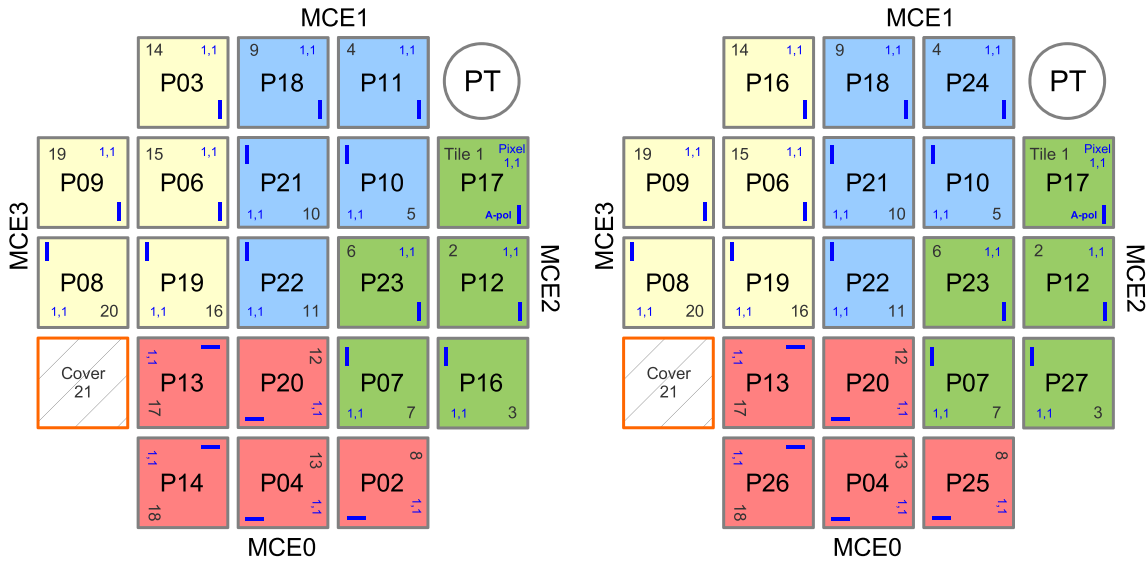

Figure 9. Left: BICEP3 focal plane layout in 2016. Right: four modules were replaced prior to the 2017 season. In each detector module, the serial number *Pxx* is labeled in the center. The orientation of the module is indicated by the pixel (1, 1) and the polarization *A* direction in blue, along with the tile number 1–20. The background color of the module indicates the four readout MCE units. The location of the pulse tube cooler is shown by the PT marking in the upper right. Slot 21, shown in an orange outline, does not contain a detector module, since the readout electronics were designed to support 20 modules. It was covered with a thin copper sheet, which created extra reflection for Tile 1 as discussed in Section 8.10.
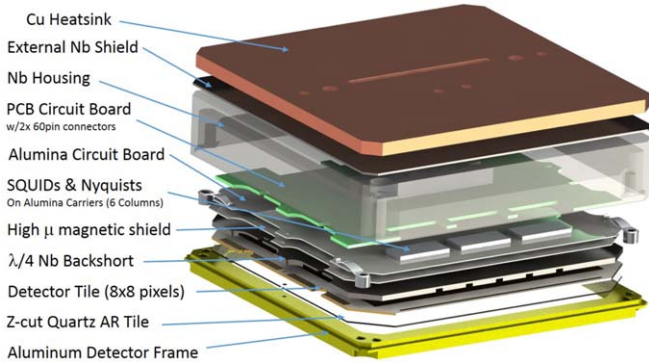

Figure 10. Exploded view of the BICEP3 detector module. Sky side is facing downward in this diagram. The multiplexing SQUIDs and circuit boards are mounted directly behind the detector wafer, separated by a $\lambda/4$ Nb backshort and A4K magnetic shield. The backside is enclosed by a Nb cover and plate for magnetic shielding.

transition begins from the center and continues radially outwards, avoiding trapped magnetic flux during cooldown.

The backside of the module is completely enclosed with an Nb housing, with only a 35×1.3 mm slit to allow the flex cables to exit the module. A 0.5 mm thick Nb sheet with an offset slit is placed at the back of the housing, creating a near continuous superconducting magnetic shield. Additionally, a sheet of high-permeability Metglas 2714A is placed 1.27 mm away from the SQUID chips inside the module to create the lowest magnetic field environment at the location of the SQUID chips (Figure 12).

5.3. Corrugated Frame

The interaction between the detector module metal frame and the edge-adjacent planar slot antenna causes differential pointing within that detector pair. Although most of the systematic errors caused by the differential pointing are

mitigated during analysis, we corrugated the frame to minimize residual beam systematics of these pixels.

The corrugated frame has $\lambda/4$ depth and pitch, and is placed $\lambda/2$ away from the closest antenna, where λ is the design band center (Soliman et al. 2018). Figure 13 presents a differential beam map model using CST Studio Suite,[40] showing a reduction in residual beam mismatch from $\sim 34\%$ with a flat frame to $\sim 6.7\%$ with the corrugated frame, evaluated over the 25% spectral bandwidth.

6. Detectors

BICEP3 inherits the planar phased-array antenna and transition-edge sensor (TES) bolometer detector technology from BICEP2 (Ade et al. 2015). The planar antenna design does not require feed horns or similar coupling optics to free space. The 95 GHz band is defined by lumped-element filters along the microstrip feed line to the bolometers. Each silicon detector tile contains an 8×8 array of pixels and each pixel is made of two colocated, orthogonally polarized subantenna networks and two TES bolometers.

Holding the edge taper on the pupil fixed, BICEP3's faster focal ratio enables a denser detector packing than the 6×6 array of pixels in each 95 GHz *Keck* detector tile.

The TES detectors are voltage-biased, providing electrothermal stability and linearity, where electrical power compensates for variation in optical power. Each TES is made up of a titanium and aluminum film in series; the titanium transition maximizes sensitivity ($T_c \approx 0.5$ K) during normal science observation, while the higher $T_c \approx 1.2$ K aluminum TES provides higher saturation power to observe high-temperature calibration sources, though at reduced sensitivity.

Together, the two independent signals from the colocated orthogonal antenna and bolometer pairs on each pixel can be

---

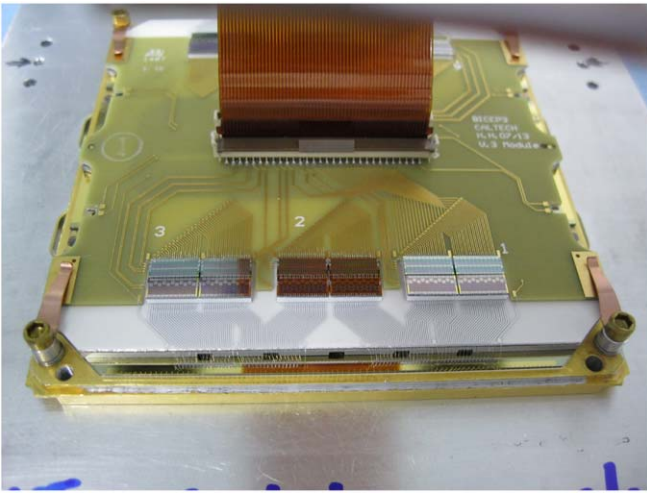[40] Dassault Systemes, www.3ds.com.

11

Figure 11. Backside of the detector module. Aluminum wirebonds connect the detectors to SQUIDs chips via an alumina circuit board. Two 60 pin Kapton/Cu flex-circuit ribbon cables connect to the ZIF connectors and travel out of the niobium casing through a thin slot to matching connectors on the focal plane board.
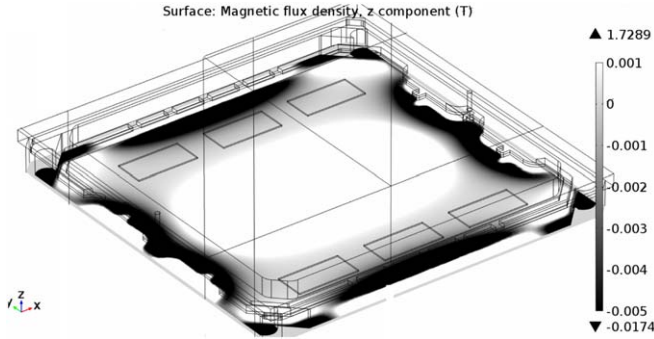

Figure 12. COMSOL Multiphysics simulation of the detector module; the scale is saturated to highlight the location of the SQUIDs (MUX). Simulation shows the external magnetic field is reduced to ~0.1% at the SQUIDs.

Figure 13. Top: simulated peak-normalized differential beam map for an edge pixel closest to the corrugation frame over 25% bandwidth at 95 GHz. Bottom: peak-to-peak differential beam amplitude over design frequency band. Solid lines are the simulated value, and dashed lines are the average value over the 25% bandwidth. Red lines show the case without metal frame, black lines show the current corrugated frame design, and blue lines show the pixel next to a solid metal wall. This modeling is confirmed by our measurements shown in Section 8.7.

summed to get total incident power or differenced to measure polarization in the vertical−horizontal direction.

6.1. Tapered Antenna Networks

Optical radiation couples to the detectors through a planar phased antenna array, combined in phase with a summing network that controls the amplitude and phase in each subslot. The illumination pattern is controlled through the microstrip feed network that sums signals from the subantennas to deliver power to the TES bolometer. Previous designs, used in BICEP2/*Keck* and SPIDER, drive each of the subantennas in phase with equal field strength, synthesizing a top-hat illumination and thus a sinc pattern in the far field. Such a pattern has sidelobes with peak levels at −13 dB below the main lobe. In these instruments, sidelobes are terminated onto the 4 K aperture stop with limited impact on the sensitivity.

Programmatically, some optical designs would benefit from lower sidelobe levels and BICEP3 was used to advance this capability. The sidelobe levels of antenna arrays can be controlled by tapering the illumination such that the central subslots have higher coupling than those at the edge. The array factor with nonuniform illumination can be generalized as
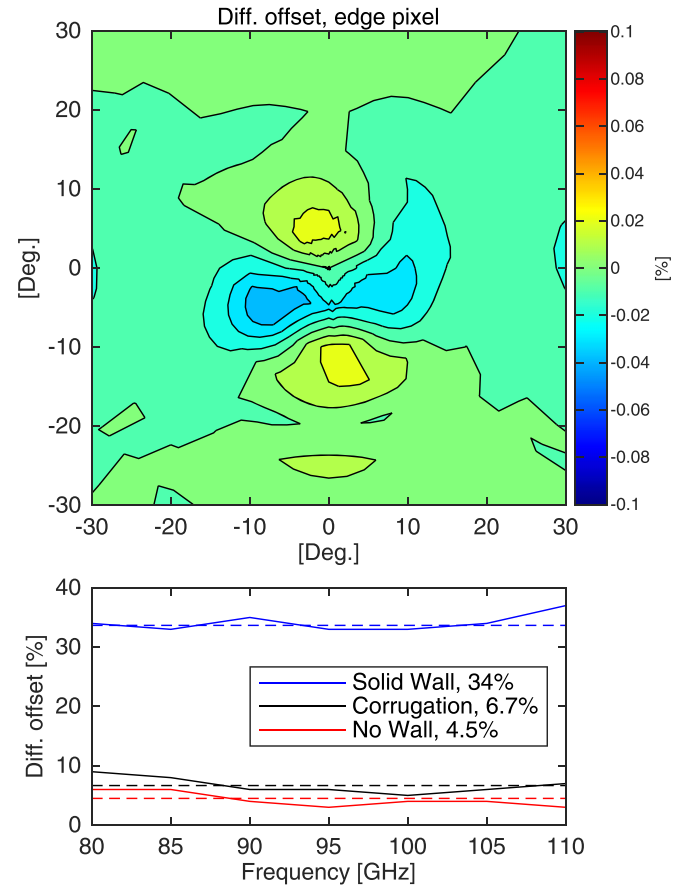
$$A(\theta) = \sum_{m=-(N-1)/2}^{(N-1)/2} E_m e^{-jmk \sin(\theta) s}$$
$$\simeq \int_S E(x', y') e^{j(k_x x' + k_y y')} \, dx' dy', \qquad (1)$$

where the last line approximates the sum as an integral across the antenna aperture, and k_x and k_y are the components of the tangential free-space wavevector $k \sin(\theta)$. This expresses the far-field antenna pattern as the Fourier transform of the illumination pattern. For BICEP3, the feed network was designed to generate a Gaussian illumination with an electric field waist radius of 6.3 mm, compared to the physical aperture size of 7.5×7.5 mm. This reduces the sidelobe levels to −16 dB and the integrated spillover to 13% compared to the 17% that would have been achieved with a uniform feed. The result is an illumination that is close to uniform, as the instrument's aperture stop requires, but also allows our team to develop flexibility for other instruments. We also developed and tested two designs with stronger tapering, which would be advantageous in optical systems with a warm pupil stop.

7. Data Acquisition System

BICEP3 uses a SQUID time-division multiplexed (TDM) system for the bolometer readout, which includes the SQUID multiplexing chips, the room-temperature Multi-Channel Electronic (MCE) system, and the overall Generic Control Program (GCP).

7.1. Time-division Multiplexing SQUID Readout

BICEP3 uses a low-noise SQUID TDM readout system, which amplifies the small current flowing through the TES while adding noise subdominant to the detector itself, and transforms the small ~60 mΩ impedance of the TES in two amplification stages. The TDM architecture is similar to that in previous experiments (de Korte et al. 2003) but uses a new generation MUX11 model that takes advantage of super-conducting-to-resistive, flux-activated switches (FSs) in the multiplexing sequence (Irwin et al. 2012). The SQUID amplifier chips were developed and fabricated by National Institute of Standards and Technology, and the operating firmware and characterization were first demonstrated in BICEP3 (Hui et al. 2016). Since then the technology has been deployed in Advanced ACTPol (Henderson et al. 2016), CLASS (Dahal et al. 2020), and BICEP ARRAY (Hui et al. 2018).

In the readout architecture each independent detector is inductively coupled to a single SQUID array (SQ1) by an input coil, and the amplifier is operated in a flux-lock loop to linearize the output and increase the dynamic range of the periodic SQUID response. As the flux from the input coil changes in response to the TES current, a compensating flux is applied by the feedback coil to cancel it. This flux feedback serves as the signal output of the TES. The second stage SQUID array (SSA) at 4 K provides additional amplification that impedance matches to the room-temperature MCE, providing ~1 Ω dynamic resistance and a ~100 Ω output impedance.

The multiplexing circuit is arranged according to "columns" and "rows" of detectors. BICEP3 uses total of four MCE, and each MCE has a readout of 660 channels, which are mapped into 30 MUX columns and 22 MUX rows (600 optical channels, 20 dark detectors, and 40 dark SQUID channels.) Multiplexing is done across rows, such that 22 channels of each column are read out in TDM sequence. The SQ1 on each column lies in series, and the entire line is resistively shunted by the FSs. The FSs are a four Josephson junction design that behaves like a SQUID with a critical current about twice the critical current of the SQ1 when no flux is applied to them. The SQ1 and FSs are shared by the same SQ1 bias line; a zero flux applied to an FS leaves it superconducting, while half of a flux quantum applied sends the FS normal with a resistance much greater than SQ1. Each FS is coupled to an input inductor, which can apply a flux and is driven by a row-selected input line (RS) that runs across columns. At a given moment in time during the multiplexing sequence, only one RS line applies a half flux quantum to the switches of its row, while the remaining 21 RS lines remain zeroed, resulting in the shared SQ1 bias current shorts through those 21 FS. The signal bypasses those SQ1s and only flows through the single SQ1 whose FS is highly resistive. The circuit diagram of the TDM system is shown in Figure 14.
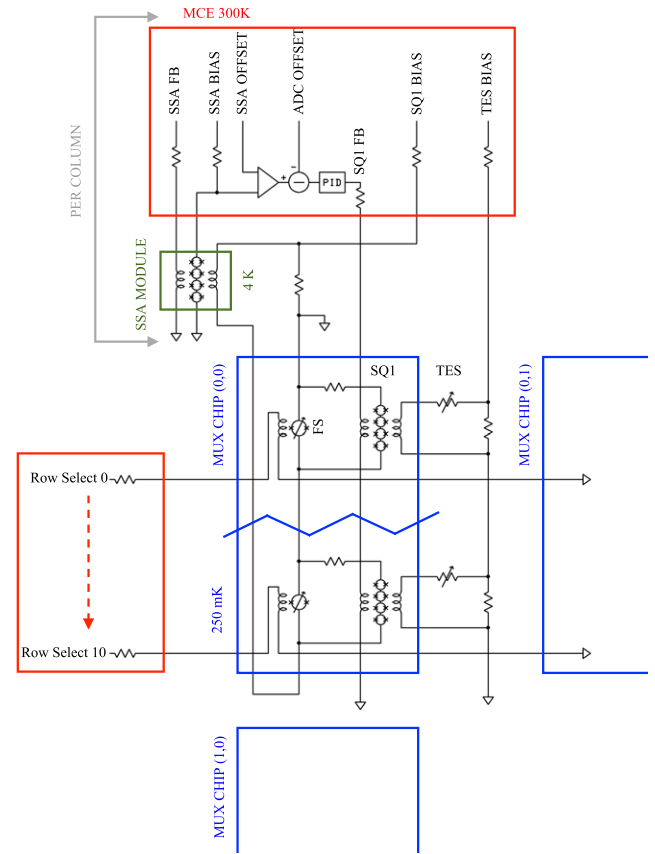

Figure 14. MUX11 SQUID readout and feedback schematic modified from Figure C.1 in Grayson (2016), explicitly showing two RSs of one MUX column. Two MUX11 chips are chained together to form the 22 multiplexing rows. Red outlines denote MCE-sourced signals at 300 K, green the SSA modules at 4 K, and blue the MUX chips at 250 mK. This diagram does not show the Nyquist chip outline or the Nyquist inductor. A single bias line is used to bias both the SQ1 and the flux switches (FSs).

Additionally, the TES bias circuits include elements of a "Nyquist" chip (NYQ), which consists of a shunt resistor $R_{sh} \sim 3$ mΩ parallel to the TES and an inductor L_{NYQ} in series with the TES. The inductor is included to create an RL filter with the TES resistance, with $L_{NYQ} \sim 2$ μH, $R_{TES} \sim 50$ mΩ resulting in a roll off at ~4 kHz to avoid aliasing of higher-frequency noise.

7.2. Warm Multiplexing Hardware

Control of the MUX system and feedback-based readout of the TES data are done via the room-temperature MCE system (Battistelli et al. 2008).

The MCE samples the raw SSA output at 50 MHz, given 90 samples each row in the MUX sequence per switch. This gives a 25.3 kHz visitation rate. The data are filtered and downsampled in the MCE before being output to the control system. The MCE uses a fourth-order digital Butterworth filter before downsampling by a factor of 168, then the the final electronic stage applies a second filtering using an acausal, zero-phase-delay finite impulse response (FIR) low-pass filter, downsampled by another factor of five, giving an archived sample rate of 30.1 Hz. The full multiplexing parameters used in BICEP3 are shown in Table 6.

Raw ADC Sample Rate	50 MHz
Row dwell	90 samples
Row switching rate	556 kHz
Number of rows	22
Same-row revisit rate	25.3 kHz
Output data rate per channel	150 Hz
Archived data rate	30.1 Hz

7.3. Control System

All of the telescope systems are controlled and read out by a set of six Linux computers running GCP, inherited and modified from BICEP/*Keck* and other CMB experiments (Story et al. 2012). These control computers interface with all telescope subsystems, including mount movement control, detectors and SQUIDs via the MCEs, and thermometry. All data timestreams are packaged into archived files on disk and streamed back with telescope operation logs to North America via daily satellite uplink. Observation and fridge-cycle scheduling are scripted within GCP and executed automatically with periodic monitoring by the operator.

8. Instrument Characterization

8.1. Detector Bands

BICEP3 detectors are designed for a frequency band centered at 95 GHz with ~25% fractional bandwidth. The band is chosen to avoid the broad oxygen absorption band around 60 GHz as well as the oxygen spectral line at 118.8 GHz.

The spectral response of each detector is measured in situ with a custom-built Martin−Puplett Fourier Transform Spectrometer (FTS) mounted above the cryostat window. The apparatus and measurement procedure are described in Karkare et al. (2014). The band center $\langle\nu\rangle$ in frequency ν is defined as

$$\langle\nu\rangle = \frac{\int \nu S(\nu)d\nu}{\int S(\nu)d\nu}, \qquad (2)$$

where $S(\nu)$ is the spectral response, and its bandwidth $\Delta\nu$ is defined as

$$\Delta\nu = \frac{\left(\int S(\nu)d\nu\right)^2}{\int S^2(\nu)d\nu}, \qquad (3)$$

where we choose to normalize the spectral response such that $\int S^2(\nu)d\nu/\int S(\nu)d\nu = 1$.

The FTS beam is smaller than the pupil, but illuminates several detectors at once in angular extent. This leads to frequency-dependent beam truncation in the measurement, with a spectral shape that depends on the beam size at the aperture, the size of the FTS entrance port, and the nominal detector frequency. A correction ν^a is applied to the final spectra $S(\nu)$, where a is calculated using models from intensity measurements over the pupil (Section 8.7). We measured a median band center at 96.1 ± 1.5 GHz with a median bandwidth at 26.8 ± 1.3 GHz, corresponding to a fractional spectral bandwidth of 27%.

The delamination of the low-pass edge filters described in Section 3.6 resulted in nonuniform spectral features in the detectors during the 2016 season (Figure 15) as well as a
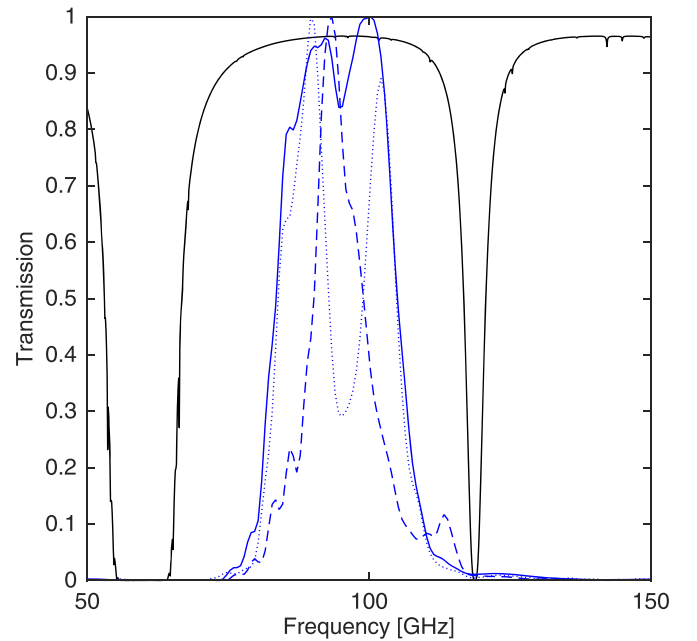

Figure 15. The peak-normalized, average spectral response of BICEP3 detectors (solid blue) shown against the atmospheric transmission at the South Pole (black). Also plotted are two extreme example cases of the type of bandpass variation caused by delamination of the low-pass edge filters in 2016: a spike-like spectrum (dashed blue, $e = -0.51$) and a dip-like spectrum (dotted blue, $e = 0.20$). All low-pass edge filters were replaced for the 2017 season, and subsequent measurements are similar to the average spectrum for all detectors.

decrease in optical efficiency. We broadly observed two types of spectral variations: one where the response was suppressed at the outer edges of the nominal band, which created a "spike" shaped profile, and one where the response was suppressed at the center of the band and created a "dip." To further characterize this feature, we define an estimator e:

$$e = \underset{\substack{84<\nu<90\text{GHz}\\98<\nu<106\text{GHz}}}{\text{mean}}[B'(\nu)] - \underset{90<\nu<98\text{GHz}}{\text{mean}}[B'(\nu)], \qquad (4)$$

where $B'(\nu) = G(\nu; \sigma)^*B(\nu)$. $B(\nu)$ is the peak-normalized detector spectral response from FTS measurements, $G(\nu; \sigma)$ is a Gaussian with $\sigma = 1$ GHz, and $B'(\nu)$ is the detector spectrum convolved with the Gaussian smoothing kernel. The estimator e takes on values $-1 \leqslant e \leqslant 1$, with $e < 0$ being spike-like and $e > 0$ being dip-like. The distribution of estimator values is shown in Figure 16. All of the low-pass edge filters were replaced at the end of the 2016 season, and no evidence of delamination has been found since their replacement. In order to determine the impact of these spectral features on the 2016 CMB data, we developed an additional jackknife test discussed further in Section 10.3.

High-frequency blue leaks originating from direct-island coupling to the TES bolometer are measured using a chopped liquid nitrogen source and a stack of thick grill high-pass filters (Timusk & Richards 1981). These filters are machined metal plates with hex-packed circular holes corresponding to waveguide cutoff frequencies at 120, 170, and 247 GHz. Measurements showed response to a Raleigh–Rayleigh source of approximately 0.76%, 0.61%, and 0.55% above the 120 GHz, 170 GHz, and 247 GHz edge, respectively.
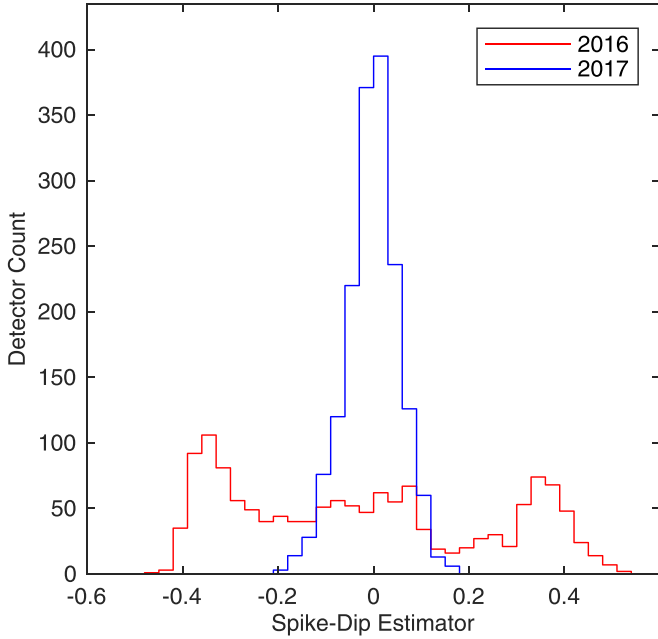
Figure 16. The spectral (spike-dip) estimator e with the 2016 and 2017 focal planes, calculated with Equation (4). The peaks at $e = \pm\sim0.4$ indicate that many detectors in the 2016 focal plane exhibited spike and dip-like features.

Figure 17. Optical efficiencies of BICEP3 detectors. The median efficiency increased from 26% in 2016 (red) to 32% in 2017 (blue). Because the optical efficiency measurement is performed with the detectors biased on the aluminum transition, the detector yield shown here is lower than the yield for CMB observations, when the detectors are biased on the titanium transition.

8.2. Optical Efficiency

We measured changes in optical power through detector load curves by applying a high detector bias voltage to first drive the detector normal, then stepping down the bias voltage until the detector is superconducting. From these load curves, we can measure changes in optical power, assuming the total optical and electrical power is constant. The power difference is compared against the expected optical loading from an aperture-filling source at a known temperature, giving the end-to-end optical efficiency of the full system.

The change in optical loading is obtained by taking load curves while observing a source at ambient temperature ($\sim$266 K) and a liquid nitrogen (LN2) source at 74.2 K (at South Pole atmospheric pressure). For an aperture-filling, Rayleigh–Jeans source, the optical power Q_{opt} deposited on a single-moded polarization-sensitive detector is

$$Q_{\text{opt}} = \frac{\eta}{2} \int \lambda^2 S(\nu) B(\nu, T) d\nu \qquad (5)$$

where η is the optical efficiency, $B(\nu)$ is the Planck blackbody spectrum at temperature T, and $S(\nu)$ is the detector spectral response. In the Rayleigh–Jeans limit ($h\nu \ll kT$), Equation (5) simplifies to

$$Q_{\text{opt}} = kT\eta \int S(\nu) d\nu = kT\eta \Delta\nu \qquad (6)$$

where $\Delta\nu$ is the bandwidth and η is the optical efficiency of the system. Observations of the sky and an aluminum mirror redirecting light into the cryostat provide estimates of the atmosphere and the internal cryostat photon load.

The BICEP3 per-detector optical efficiencies as measured using this method are shown in Figure 17. The median end-to-end optical efficiency improved from 26% in the 2016 season to 32% in 2017. This is mostly due to the change in 300 K thermal filters described in Section 3.3 and the replacement of
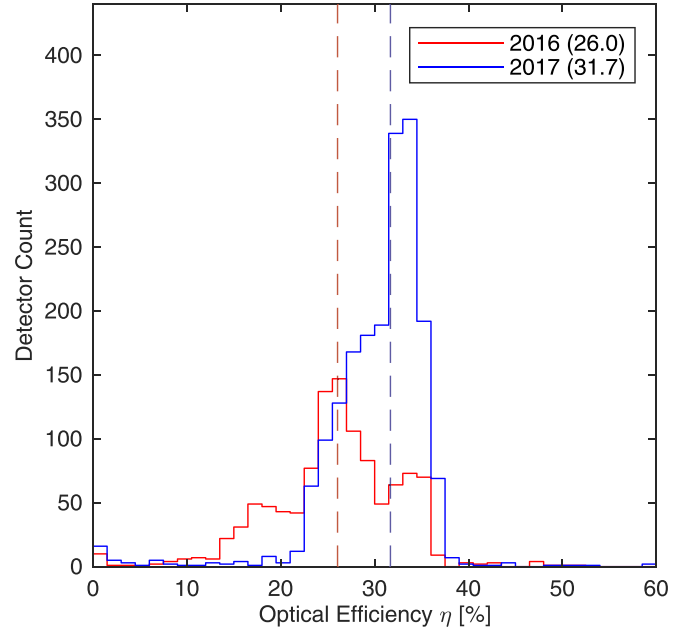
the delaminated metal-mesh edge filters described in Section 3.6.

8.3. Measured Detector Properties

We designed the thermal conductance of the detector to avoid saturation during science observations while minimizing phonon noise. The design saturation power of the BICEP3 detectors is 5 pW, which has a safety factor of 2–2.5 from the expected optical load during nominal observing conditions, giving a target thermal conductance $G_c = 40 \text{ pW K}^{-1}$ for the titanium TES bolometer with transition temperature $T_c = 500$ mK and bath temperature $T_o = 280$ mK, where we assume a thermal index $\beta \sim 2$ from bare silicon nitride supports.

The detectors are screened prior to deployment to ensure that the properties are near target values. The thermal conductance G_c, thermal conductance index β, and transition temperature T_c are given by

$$P_{\text{sat}} = G_c T_o \frac{(T_c/T_o)^{\beta+1} - 1}{\beta + 1}, \qquad (7)$$

where P_{sat} is the saturation power of the detector. These parameters, shown in Table 7, are measured by taking load curves at multiple bath temperature T_o in a "dark" configuration, where the cryostat is optically sealed to prevent light coupling to the detectors.

The effective thermal time constant τ of an ideal voltage-biased TES bolometer is given by

$$\tau = \frac{C/G}{1 + \mathscr{L}(V)}, \qquad (8)$$

where C is the heat capacity of the bolometer island and $\mathscr{L}$ is the effective loop gain of the electrothermal feedback at detector bias voltage V. The detector time constants τ in BICEP3

Table 7
Average Detector Parameters for Each BICEP3 Module

Module	Norm. Rest.	P$_{sat}$ at 300 mK	Thermal Conductance	Tran. Temp.	Band Center	Bandwidth
(P02)	81 mΩ	3.71 pW	27.2 pW K^{-1}	503 mK	91 GHz	19 GHz
(P03)	83 mΩ	3.01 pW	39.1 pW K^{-1}	514 mK	94 GHz	22 GHz
P04	92 mΩ	4.76 pW	41.2 pW K^{-1}	492 mK	94 GHz	23 GHz
P06	65 mΩ	4.25 pW	32.5 pW K^{-1}	501 mK	93 GHz	24 GHz
P07	61 mΩ	4.56 pW	32.1 pW K^{-1}	507 mK	95 GHz	25 GHz
P08	63 mΩ	4.33 pW	32.2 pW K^{-1}	505 mK	92 GHz	22 GHz
P09	63 mΩ	5.61 pW	46.5 pW K^{-1}	479 mK	93 GHz	23 GHz
P10	49 mΩ	5.03 pW	35.4 pW K^{-1}	513 mK	93 GHz	24 GHz
(P11)	138 mΩ	6.72 pW	72.4 pW K^{-1}	478 mK	92 GHz	21 GHz
P12	78 mΩ	5.57 pW	41.1 pW K^{-1}	494 mK	92 GHz	22 GHz
P13	78 mΩ	5.97 pW	46.1 pW K^{-1}	487 mK	93 GHz	26 GHz
(P14)	153 mΩ	…	…	…	92 GHz	22 GHz
P16	91 mΩ	4.71 pW	31.6 pW K^{-1}	474 mK	95 GHz	18 GHz
P17	105 mΩ	4.22 pW	56.2 pW K^{-1}	452 mK	93 GHz	20 GHz
P18	86 mΩ	4.41 pW	36.4 pW K^{-1}	458 mK	95 GHz	23 GHz
P19	73 mΩ	4.03 pW	31.3 pW K^{-1}	438 mK	93 GHz	24 GHz
P20	79 mΩ	4.41 pW	32.4 pW K^{-1}	460 mK	93 GHz	22 GHz
P21	74 mΩ	4.16 pW	32.3 pW K^{-1}	474 mK	95 GHz	26 GHz
P22	72 mΩ	5.71 pW	46.4 pW K^{-1}	485 mK	93 GHz	21 GHz
P23	70 mΩ	5.14 pW	42.3 pW K^{-1}	484 mK	93 GHz	24 GHz
P24	59 mΩ	3.05 pW	26.4 pW K^{-1}	483 mK	93 GHz	24 GHz
P25	64 mΩ	4.20 pW	32.7 pW K^{-1}	461 mK	93 GHz	24 GHz
P26	49 mΩ	3.34 pW	24.9 pW K^{-1}	479 mK	93 GHz	24 GHz
P27	62 mΩ	3.14 pW	27.2 pW K^{-1}	474 mK	93 GHz	24 GHz

Note. Four of the modules, listed in parentheses, were replaced before the 2017 season. The normal resistance, saturation power, thermal conductance, and transition temperature are measured in a dark TES configuration before deployment for this subset of modules. The optical efficiency and spectral response were measured in situ at the South Pole. Figure 9 shows the placement of the detector modules over the focal plane.

are calculated by measuring the detector response to square-wave modulations in the bias voltage (Figure 18).

8.4. Detector Bias

The detectors operate in strong electrothermal feedback to linearize the response and to speed up the time constant. The usable bias range is limited by thermal instability at low bias, and detector saturation at high bias as shown in Figure 19. We believe thermal instability arises from finite thermal conductivity internal to the island, which becomes problematic at the higher backgrounds at higher observing frequencies (Sonka et al. 2017).

The sensitivity of the detectors as a function of bias voltage is measured before each observing season to select the optimal bias. This is done by taking three-minute "noise stares" with the telescope at the nominal elevation for CMB observation, and comparing the noise levels obtained with the optical response as inferred from elevation nods (described in further detail in Section 9.3). Due to the multiplexing design, all detectors in one readout column share a common bias voltage. This limitation only modestly reduces system sensitivity, as the per-detector NET is sufficiently insensitive to bias to allow a wide range of operating bias points.

8.5. Crosstalk

Crosstalk can occur between neighboring detectors within a readout column in the TDM system. One way to quantify the level of crosstalk through the readout chain is using cosmic rays. When a cosmic ray hits a detector, it generates a transient

signal that may also trigger a faint signal in neighboring detectors in a readout column. We set up a custom analysis that searches unfiltered data to locate spikes from cosmic rays, stacks multiple events to increase the signal-to-noise ratio, and compares the response in neighboring channels. Through this analysis, we find the crosstalk level in BICEP3 is consistent with previous experiments at ∼0.3%. The fact that upstream is very similar to downstream crosstalk (see Figure 20) argues that inductive crosstalk dominates over settling time crosstalk. The CMB temperature-to-polarization leakage due to crosstalk is quantified in the beam simulations shown in Appendix F of BICEP/Keck et al. (2021).

8.6. Timestream Noise

While the science audio band in BICEP3 is ∼0.1–1 Hz, the TDM readout system can alias higher-frequency noise at multiples of the multiplexer's Nyquist frequency into the science band. So we must model this high-frequency noise, particularly in our readout electronics, and check that aliased noise does not compete with photon and phonon noise.

Figure 21 shows the noise spectrum of a single detector under nominal observing conditions, as well as a model of the component contribution. The photon noise is

$$\text{NEP}^2_{\text{photon}} = 2h\nu Q_{\text{load}} + \frac{2Q^2_{\text{load}}}{\nu\frac{\Delta\nu}{\nu}}, \qquad (9)$$

where ν is the frequency, $\frac{\Delta\nu}{\nu}$ is the fractional bandwidth, and Q_{load} is the sum of astrophysical, atmospheric, and internal cryostat power loading. Table 4 summarizes all optical sources
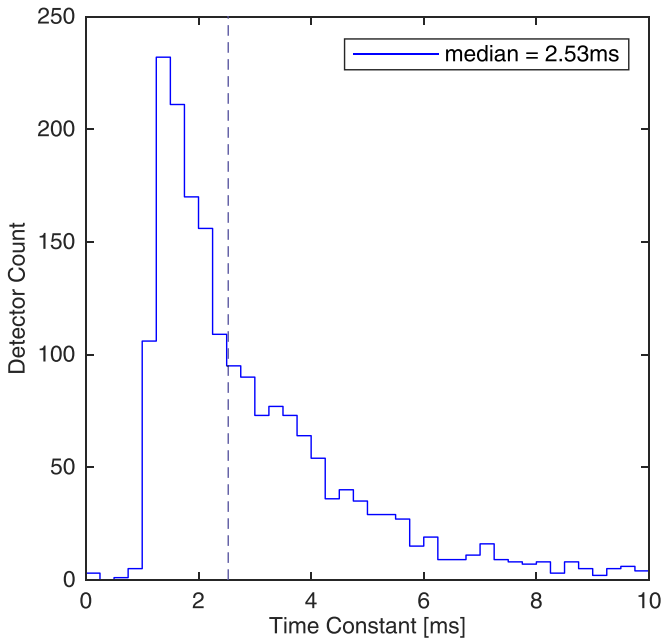
Figure 18. Detector time constants in 2021, measured at the nominal TES bias voltage used for CMB observations.
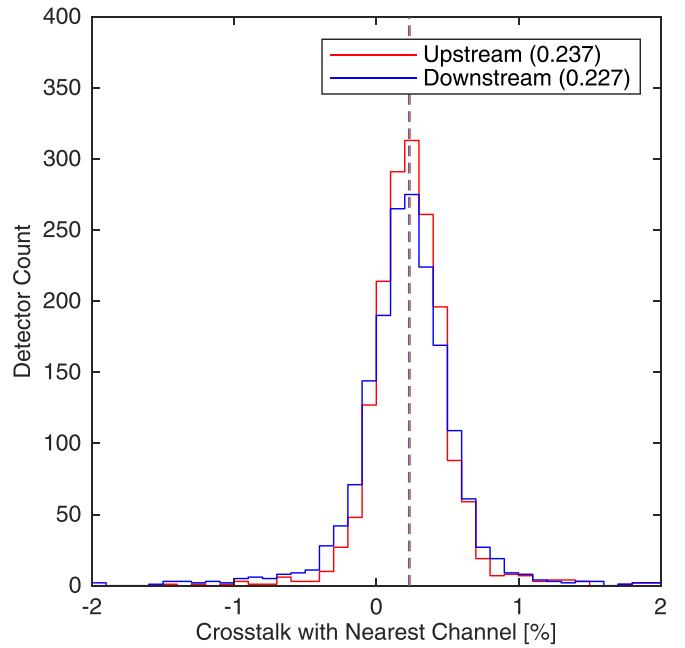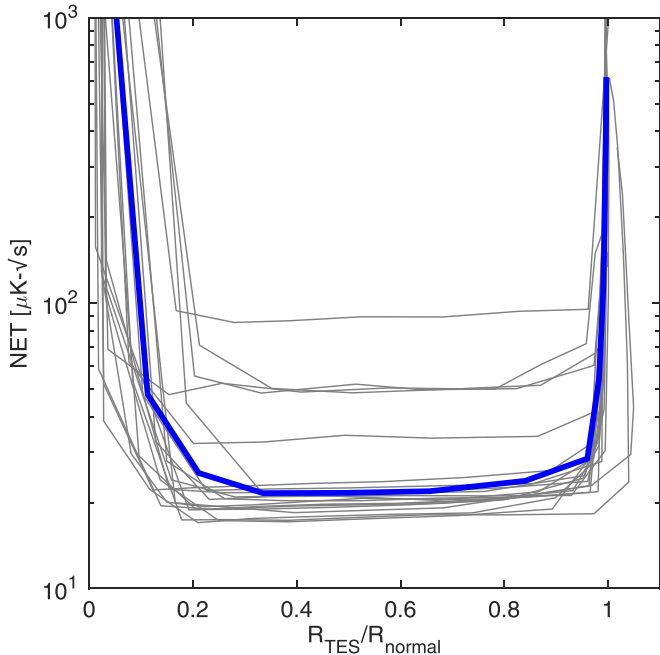

Figure 19. Noise equivalent temperature (NET) in units of CMB temperature as a function of detector resistance. The gray lines are the NET for each detector in one sample readout column, and the blue line is the average response for that column. The optimal bias point for the readout column is determined when average NET is at its minimum. The "noise stares" were taken under conditions of low atmospheric loading with an assumed sky temperature. Variation in sky temperature will affect the absolute NET values shown in this figure, but do not impact the selection of optimal bias point.

that contribute to Q_{load}, dominated by the atmosphere. The computed photon noise dominates over the other internal noise mechanisms in the detector and electronics (Irwin & Hilton 2005). The next most significant noise contribution comes from phonon noise,

Figure 20. Measured nearest-neighbor crosstalk in each detector using a cosmic-ray analysis with median value shown in parentheses. The red histogram shows upstream crosstalk (response seen in the detector visited before the target detector in the time domain) and the blue histogram shows downstream crosstalk (response seen in the detector sampled after the target detector).

$$\mathrm{NEP}^2_{phonon} = 4kT_c^2 G_c F(T_c, T_{bath}),\qquad(10)$$

where G_c is the thermal conductance, and $F(T_c, T_{bath})$ accounts for the distributed thermal conductance and is estimated to be $\sim$0.5. The Johnson noise, suppressed by the TES thermal feedback loop gain $\mathscr{L}$, and the SQUID amplifier noise are subdominant at low frequencies.

As seen in Figure 21, the measured total noise exceeds the calculated total at frequencies $\geqslant$100 Hz. This excess noise lies above that predicted by simple noise models, and tends to be proportional to the slope of the superconducting transitions as described in Gildemeister et al. (2001). However, by setting the multiplexing rate to 25 kHz, we minimize aliasing most of this excess noise into the science audio band, leading to only a small contribution to the overall sensitivity (discussed in Section 10.4). Fortunately, BICEP3's parameter choices with relatively low G and relatively high multiplexing rate avoid the level of aliased excess noise observed in comparable experiments (Ade et al. 2015).

8.7. Near-field Beam Mapping

We measured the near-field angular response above the BICEP3 window during the austral summer at the South Pole in 2016 and 2017. These maps were obtained 53.5 cm above the primary lens (pupil), and represent a truncated map of the antenna response of each focal plane detector in its far field. These maps allow us to probe for various pathologies endemic to both the focal plane and optical elements before an extensive mapping campaign of the telescope far-field beams. The near-field beam maps are measured by observing a chopped $\sim$500 K thermal source that is mounted on linear translation stages that allow for X/Y motion just above the aperture plane. The mapping apparatus is mounted directly
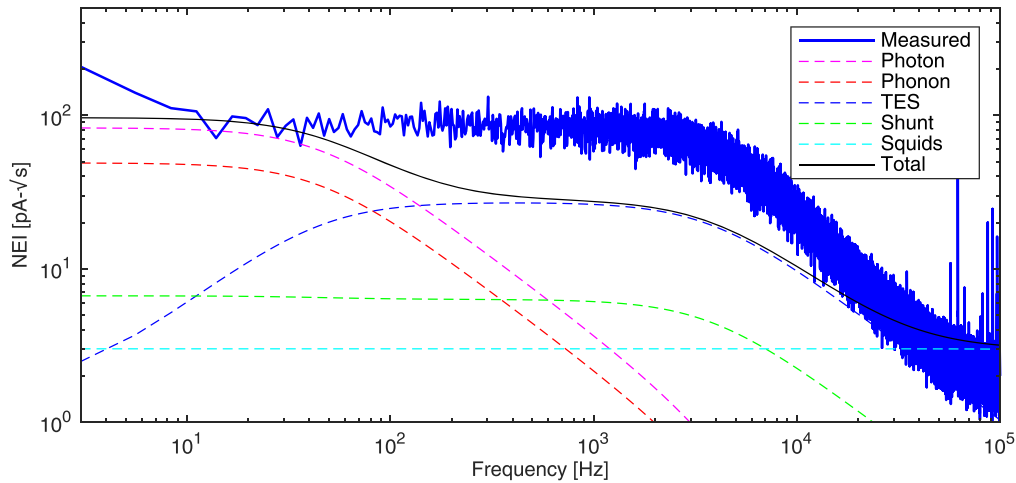
Figure 21. Measured and modeled noise for a nominal single undifferenced detector in BICEP3. We plot noise equivalent current (NEI) in the SQUID and readout electronics. The noise in Equations (9) and (10) have NEP = NEI/S, where the responsivity $S = dI/dP = 1/V * \mathcal{L}/(\mathcal{L} + 1) * 1/(1 + j\omega\tau)$, $\mathcal{L} \geqslant 10$, and the effective time constant τ is measured to be $\tau \sim 2$ ms (Figure 18). The 1/f knee at 8 Hz in the measured spectra is from atmospheric fluctuations, which are suppressed by more than an order of magnitude down to 0.1 Hz after pair-difference polarization pairs (see Figure 33).
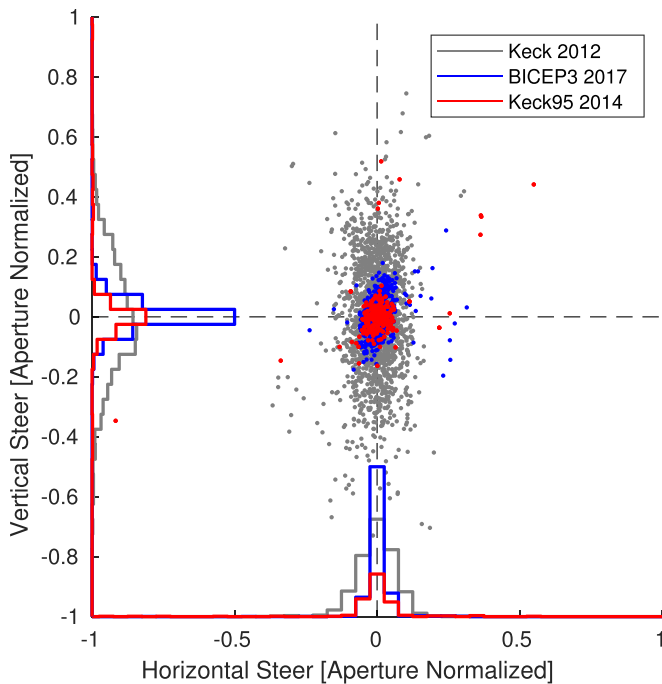

Figure 22. Near-field beam centers of BICEP3 detectors for the 2017 observing season (blue) compared to those of all *Keck* 150 GHz focal planes in 2012 (gray) and all *Keck* 95 GHz focal planes in 2014 (red). The new "etch-back" procedure in detector fabrication was implemented after 2012.

onto the window such that the hot source is placed as close to the aperture stop as possible without incurring damage to the polyethylene vacuum window. The source is scanned across the plane of the aperture in a 50 × 50 grid. At each step in this grid, the source remains stationary for ∼10 s before proceeding to the next step.

Some BICEP2 and early *Keck* detectors demonstrated off-center near-field beam centers with a large truncation at the aperture stop, which both introduced distortions in the far-field beams and reduced the optical efficiency (Wong 2014). This effect was traced to niobium contamination from the liftoff process during detector fabrication that introduced a phase shift across the planar antennas. Changing the fabrication to an "etch-back" process drastically reduced beam steer in *Keck* focal planes thereafter, and the same etching process was used in fabrication of BICEP3 modules (Buder et al. 2014). Figure 22 shows beam steer measured across all detectors of BICEP3 compared to all detectors of the 95 GHz focal planes on *Keck* (both using the new etching process) and to *Keck* 150 GHz detectors (using the old process). While some beam steer still exists, the improved fabrication method led to a significant reduction in beam truncation at the aperture stop.

These measurements also characterize the mismatch in near-field beam centers between detectors within a given pair, which can arise either from a preferential steering of one detector in a pair, or from interactions between a detector at the tile edge and the surrounding corrugated frame (see Section 5.3). As shown in Figure 23, a detectable increase in mismatch can be seen in detectors close to the corrugation frame that is at a level consistent with the simulations shown in Figure 13. Combining this near-field beam map data set with metrics derived from the far-field beam maps described in Section 8.8, we found no significant correlation between near-field beam steer and far-field beam shape in detectors that contribute to the final CMB data set.

8.8. Far-field Beam Mapping

Prior to the start of each observing season, BICEP3 undergoes an extensive far-field beam mapping (FFBM) campaign to characterize the shape of each beam in the telescope far field. The compact aperture allows measurement of the far field (∼170 m for BICEP3) by placing a chopped source on a nearby ground-base location, the adjacent Martin A. Pomerantz Observatory (MAPO) building (where *Keck* was, and BICEP ARRAY is, stationed), 200 m away from BICEP3. A 1.7 × 2.5 m flat aluminum mirror is erected at a 45° angle above BICEP3, allowing the telescope to observe the source that is otherwise obstructed by the ground shield. The source is mounted on a 40 ft vertical mast above MAPO, consisting of a 24 inch aperture that is chopped between an ambient blackbody (∼250 K) and the sky at zenith (∼10 K). Details of the setup and results of the pre-2016 season measurement are found in Karkare et al. (2016).
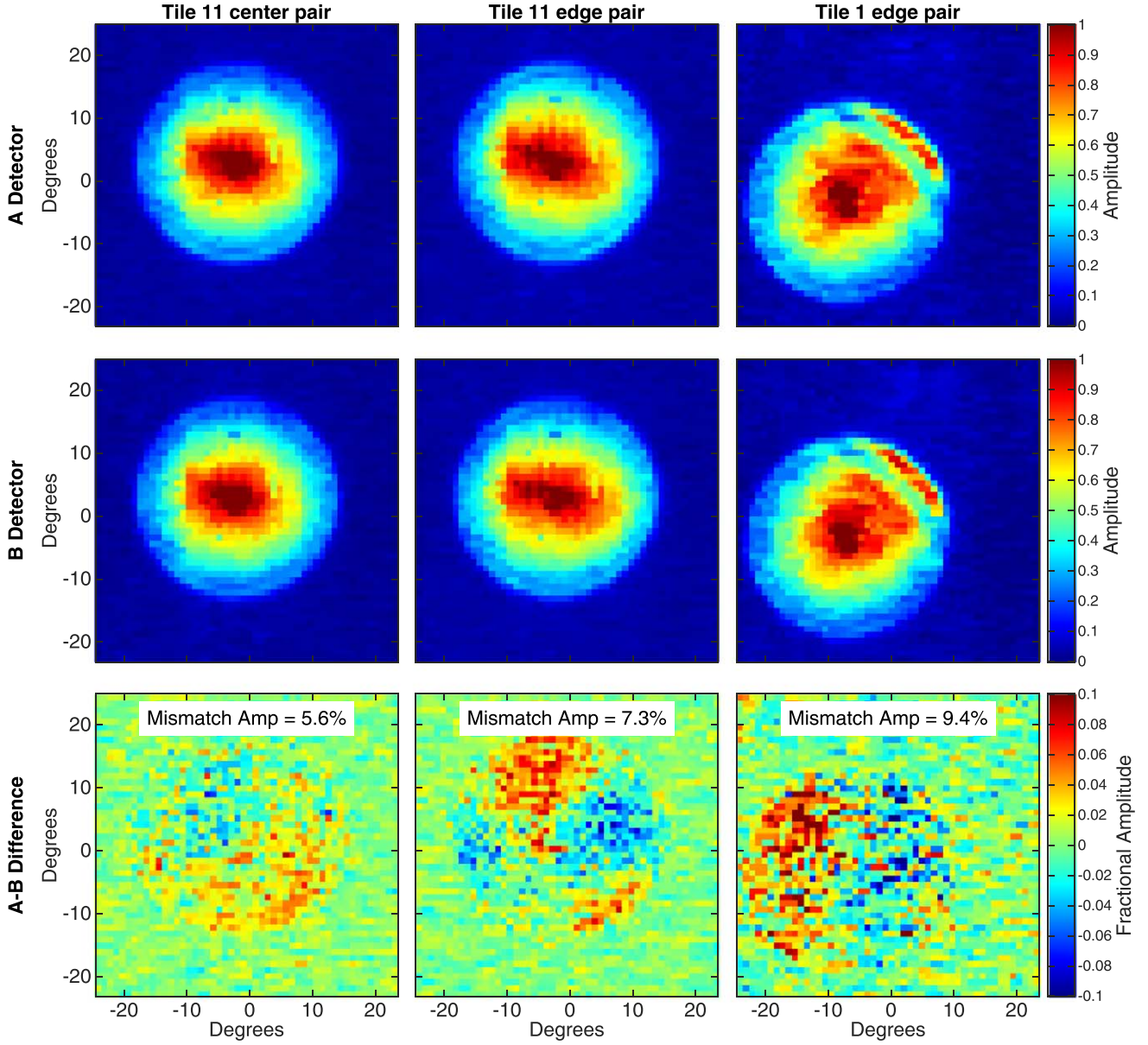
Figure 23. Amplitude-normalized near-field beam maps for detector pairs individually (top and middle rows) and their difference beams (third row) for a pair at the center of both the focal plane and its respective tile (left column); a pair near the center of the focal plane but at the edge of its tile (middle column); and a pair that is both at the edge of its tile and the whole focal plane. The pair centered both in the tile and focal plane demonstrates the minimum typical A/B mismatch that can be expected by detectors under ideal conditions. The pairs central on the FPU but at the edge of the tile confirms both the level and shape of the simulations in Figure 13 where differential pointing is slightly exacerbated by the proximity of a detector pair to the corrugation frame. The pair at the edge of both the FPU and its tile demonstrates how a small subset of beams near the edge are steered into the aperture stop, which we attribute to beam truncation at the camera lens.

The raw beam map timestreams are demodulated at the chop rate to isolate the signal from the chopped source, and are binned into per-detector maps with 0.1 square degree pixels, that we hereafter refer to as component maps. Each beam is then fit to a 2D elliptical Gaussian:

$$B(\boldsymbol{x}) = \frac{1}{\Omega} e^{-\frac{1}{2}(\boldsymbol{x}-\boldsymbol{\mu})^T \Sigma^{-1}(\boldsymbol{x}-\boldsymbol{\mu})}, \tag{11}$$

where $\boldsymbol{x}$ is the two-dimensional coordinate of the beam center, $\boldsymbol{\mu}$ is the origin, Ω is the normalization, and Σ is the covariance matrix, defined as

$$\Sigma = \begin{pmatrix} \sigma^2(1+p) & c\sigma^2 \\ c\sigma^2 & \sigma^2(1-p), \end{pmatrix} \tag{12}$$

where σ is the beamwidth, and p and c are plus and cross ellipticity, respectively. The fit values for BICEP3 are shown in Table 8 where the individual measurement uncertainty is the spread in parameter values over all component maps for a given detector, and is generally smaller than the detector-to-detector scatter. The median Gaussian beamwidth for BICEP3 is 0.161°, equivalent to an FWHM of 0.379°.
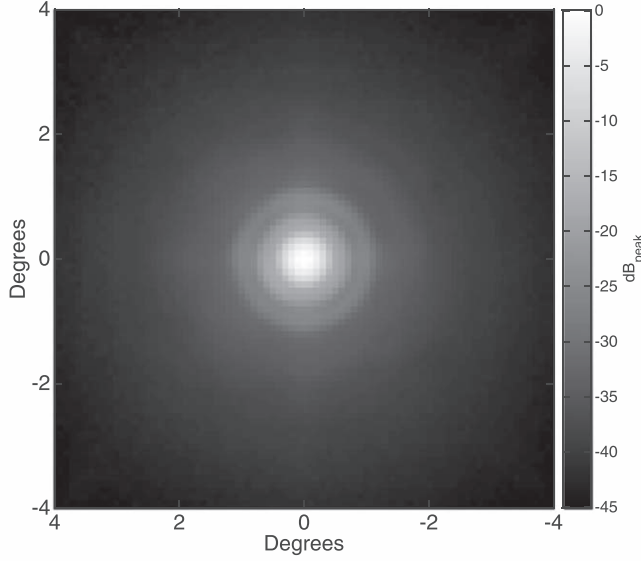
Figure 24. The BICEP3 average beam, made by coadding composite beam maps from all optically active detectors.
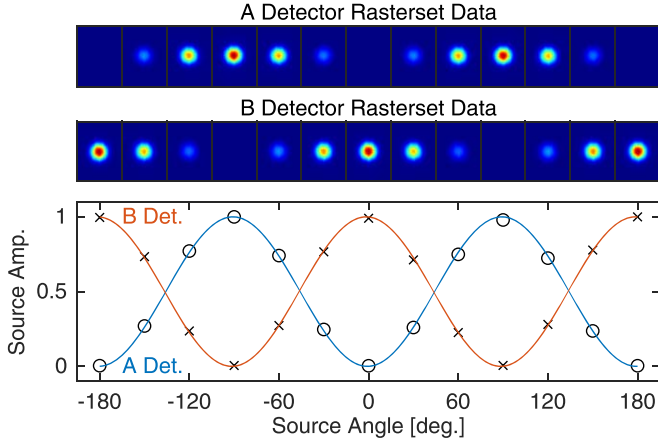

Figure 25. Beam maps of individual RPS rasters for an A/B-polarization detector (top/middle) and the corresponding normalized modulation curve (bottom), where the blue and orange lines are the best fits to the A- and B-polarization detectors, respectively.

Table 8
BICEP3 Median Far-field Beam Parameters

Parameter	Median ± Scatter ± Unc.
Beamwidth σ (degrees)	$0.161 \pm 0.003 \pm 0.001$
Ellipticity plus p	$0.008 \pm 0.002 \pm 0.002$
Ellipticity cross c	$-0.010 \pm 0.020 \pm 0.019$
Diff. beamwidth $d\sigma$ (degrees)	$0.000 \pm 0.001 \pm 0.001$
Diff. ellipticity plus dp	$-0.003 \pm 0.011 \pm 0.002$
Diff. ellipticity cross dc	$-0.003 \pm 0.004 \pm 0.002$
Diff. pointing dx (arcmin)	$-0.060 \pm 0.120 \pm 0.050$
Diff. pointing dy (arcmin)	$0.000 \pm 0.130 \pm 0.050$

Note. These values are taken from 2017 FFBM data and are presented as median over all detectors ± scatter over all detectors ± individual measurement uncertainty.

The component beam maps for each detector are then averaged together to create high-fidelity, per-detector composite beam maps. These composite beam maps are then coadded
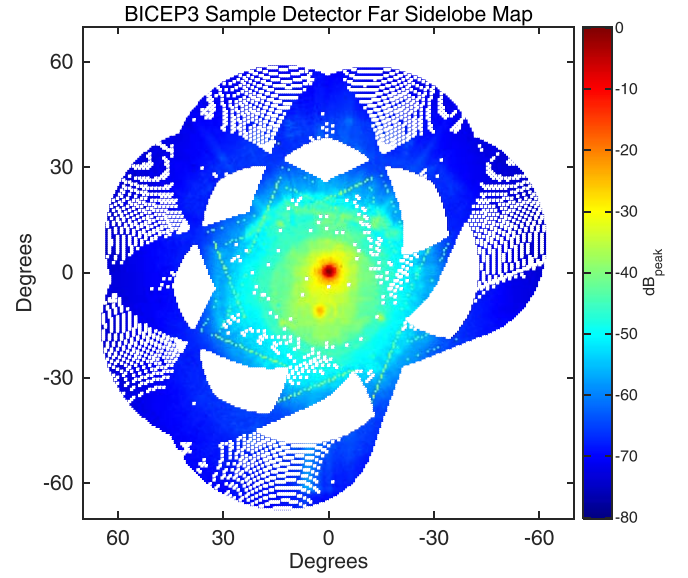

Figure 26. Sample far-sidelobe map of a BICEP3 detector, made by stitching together measurements from three power settings and coadding maps made at both source polarization orientations. The forebaffle was on for this measurement, representing the true beam response on sky as during CMB observations. The main beam and extent of the BICEP3 aperture are clearly seen. The feature just below the main beam in the map is the "ghost" beam described in the text.
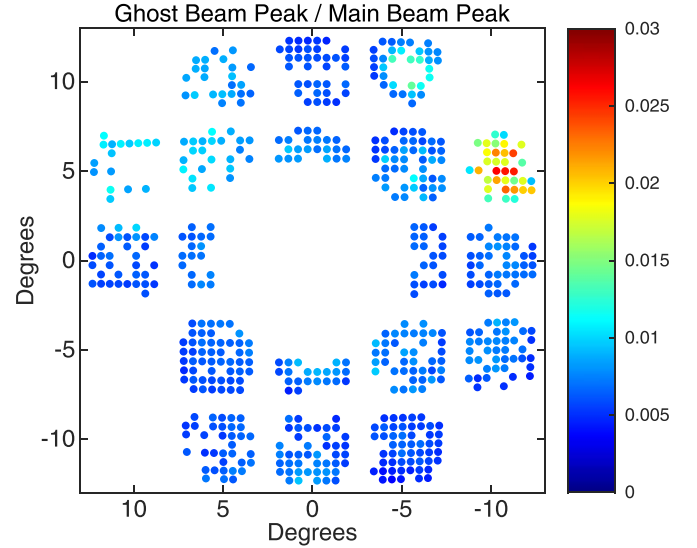

Figure 27. Per-pair values of the ratio of ghost beam peak power to the main beam peak power. Each point is the average between both detectors in a pair. For detectors near the center of the focal plane, ghost beams cannot be confidently separated from the main beam and are therefore omitted from this plot. Tile 1 (top-right corner) has higher-amplitude ghost beams due to the increased reflection from the blanked port on the opposite side of the focal plane.

over all detectors to form the receiver-averaged beam, shown in Figure 24. The receiver-averaged beams are then Fourier transformed and azimuthally averaged into the beam window function $B(\ell)$, which is inverted to recover the sky power spectrum. The per-detector composite beams are also used to quantify the temperature-to-polarization leakage in a given data set, which is done in Appendix F of BICEP/Keck et al. (2021).
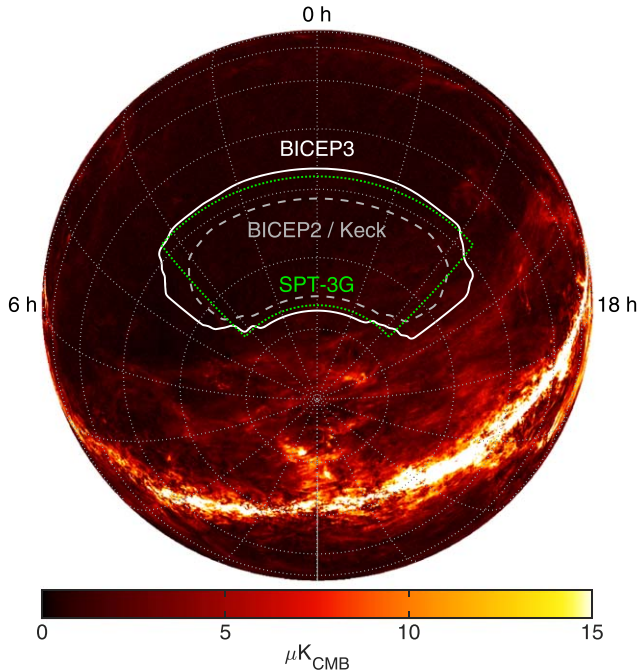
Figure 28. The BICEP3 CMB observing field (solid white) on the southern celestial sphere, together with the smaller BICEP2/*Keck* field (dashed white) and the SPT-3G 1500 deg^2 survey (dotted green; Sobrin et al. 2021). The background image shows the polarized intensity $P = \sqrt{Q^2 + U^2}$ of the *Planck* component-separated (SMICA) dust map (Planck Collaboration et al. 2020b), rescaled in amplitude from 353 GHz to 95 GHz assuming a graybody spectrum with temperature $T_d = 19.6$ K and spectral index $\beta_d = 1.5$.

Table 9
Observation Schedule for BICEP3

Phase	LST	Field	No. of Scansets
A	Day 0 23:00	Fridge re-cycling	
B	Day 1 05:00	CMB	10
C	Day 1 14:00	CMB	10
D	Day 1 23:00	Galactic	7
E	Day 2 05:00	CMB	10
F	Day 2 14:00	CMB	10
G	**Day 2 23:00**	**CMB**	**6**
H	**Day 3 05:00**	**CMB**	**10**
I	**Day 3 14:00**	**CMB**	**10**

Note. Start times are listed by Local Sidereal Time (LST). The 2016 season used a two-day schedule without the bolded phases G, H, and I.

cross-polar response of each detector, which is dominated by the crosstalk between the two detectors within a pair. The median cross-polar response is measured to be $0.7\% \pm 0.2\%$, consistent with the crosstalk within the measurement uncertainty. While any difference between the measured and assumed cross-polar response contributes to additional uncertainty on the absolute gain calibration of the *E*- and *B*-mode polarization maps, it does not introduce any additional bias in the *B*-mode signal.

8.10. Far-sidelobe Mapping

All BICEP/*Keck* receivers use two levels of warm baffling to ensure that any ray must diffract twice to couple to the ground as described in Section 2.3. Any excess power in the far sidelobe (FSL; roughly defined as the part of the beam outside the region captured by the comoving forebaffle) should be coupled to an ambient-temperature absorber or redirected via the ground shield to cold sky. However, this power still increases the loading of the detectors, and if polarized, could lead to leakage that may be difficult to constrain. We therefore take measurements using a high-powered noise source to map the far-sidelobe region response. This measurement used the same noise source described in Section 8.9, which has variable attenuation that gives ~70 dB of dynamic range needed to map out all regions of the beam. The source is mounted on a mast on the same building as the BICEP3 instrument.

A typical far-sidelobe schedule takes 380° scans in azimuth, with an elevation range of 34° in 0.5° steps, all repeated over multiple boresight rotation angles. The measurement is often repeated with both the comoving forebaffle on and off, as an external check of the amount of power intercepting the forebaffle. A waveguide twist can be placed before the source output horn that couples to free space, in order to take measurements in two orthogonal source polarizations. Three different power settings are used to map out the entire beam at each boresight rotation angle, where the power settings are changed by adjusting the attenuation in the source. A "low" power setting maps the main beam, "medium" maps the mid sidelobe, and "high" maps the far sidelobe. The maps made with each setting are stitched together to create a single map for each detector. The maps at each polarization (made with and without the waveguide twist installed) can be coadded together to create an effective unpolarized FSL map. An example of this for a single BICEP3 detector is shown in Figure 26.

The FSL maps also reveal a small-amplitude, well-formed "ghost beam" located on the opposite side of the boresight from

8.9. Polarization Response

Unlike previous generations of BICEP receivers, BICEP3 did not use an aperture-filling rotating polarized source as shown in Takahashi et al. (2010). Instead the polarization response is acquired through observations of a rotating polarized quasi-thermal noise source (RPS). The source is placed on the same mast used in far-field beam measurements and observed via the large flat mirror described in Section 8.8. For a single observation, maps are created by rastering across the RPS in azimuth and stepping in elevation while keeping the polarization axis of the RPS at a fixed angle. Thirteen beam maps are created for RPS angles spanning 360° in 30° increments. Figure 25 shows the resulting modulation in amplitude of the beams as a function of source polarization angle that produces a sinusoidal curve from which we derive detector polarization properties. The details and results from the RPS observations used here are described in Cornelison et al. (2020).

The relative polarization angles between detector pairs are measured to a precision of <0.04°, with a measured variation among pairs within each tile of 0.13° rms, and variation of the median angles across tiles of 0.32° rms. The small size of these variations allows us to use ideal, rather than measured, per-detector polarization angles when creating BICEP3's CMB polarization maps. Global polarization rotation is not as well constrained due to systematics arising in the geometry of the calibration itself. Instead, we estimate and subtract the global rotation angle from an *EB*/*TB*-minimization procedure to mitigate false *B*-mode signals (Kaufman et al. 2014).

The relative calibration of the polarization maps to the CMB temperature map shown in Section 9.3 depends on the level of
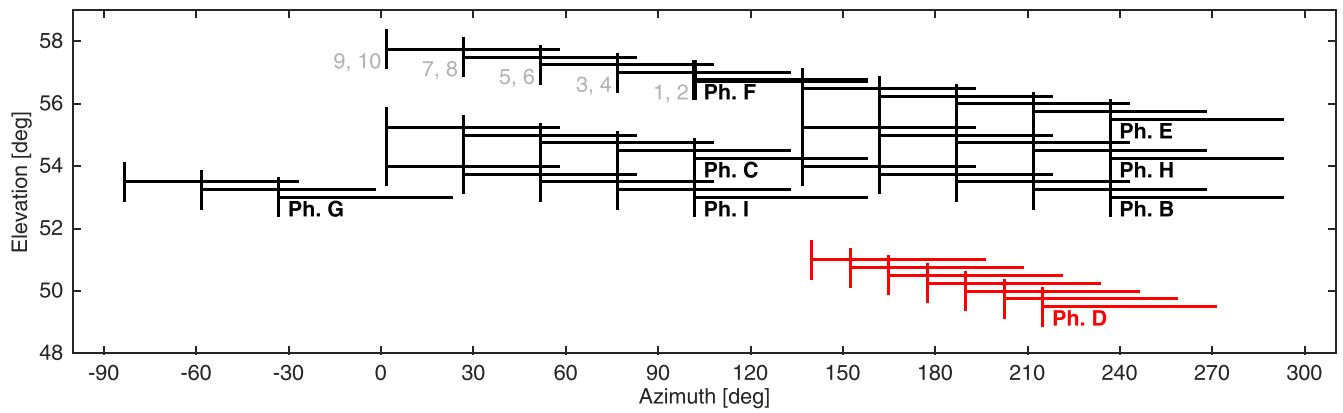
Figure 29. Observing pattern of a typical three-day schedule in ground-based coordinates. The first scanset of phase F is shown in bold. Horizontal lines indicate the field scans and the vertical lines indicate the bracketing elevation nods. The telescope scans at a fixed elevation during each scanset. For the CMB field scans, we observe two scansets before changing elevation. Phase D is on the Galactic plane.
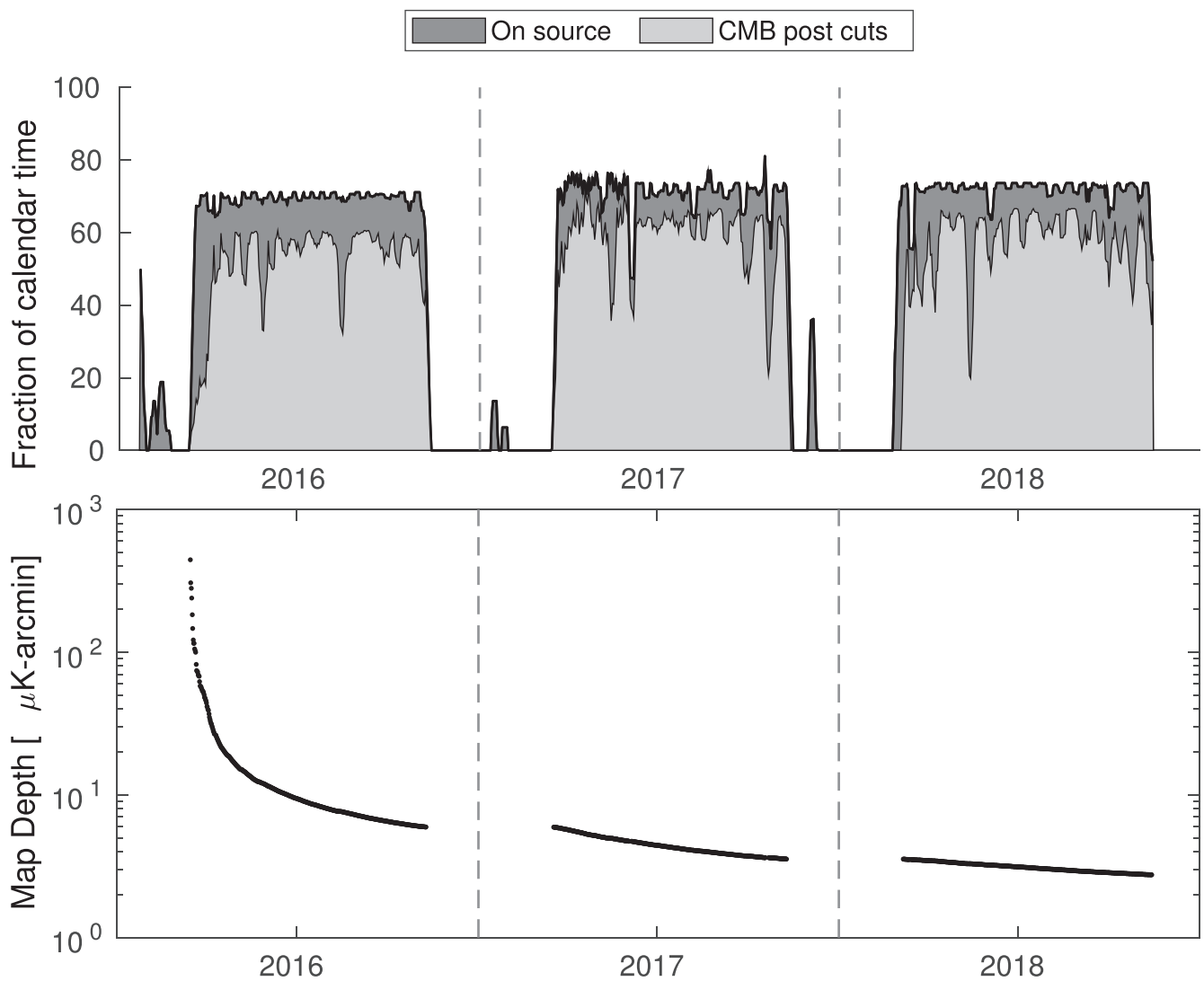

Figure 30. Integration of the BICEP3 data set from 2016 to 2018, plotting (top) fraction of time per day spent in CMB scans, excluding regular calibrations and refrigerator cycling. During austral summers (November to February), the observing schedules were interspersed with calibration measurements. During the austral winter, on-source efficiency is about 70%. The lower curve includes data quality cuts, but excludes nonfunctioning channels (Row 2 in Table 10.) The rms map-based sensitivity (bottom) improves over time and reaches 2.8 μK arcmin^{-1} at the end of 2018.

Table 10
Data Cuts as Described in Appendix A of Willmert (2019)

Cut Parameter	2016 Cuts (%)		2017 Cuts (%)		2018 Cuts (%)	
	Raw	Remaining	Raw	Remaining	Raw	Remaining
Before cuts	⋯	100.0	⋯	100.0	⋯	100.0
Nonfunctional detectors	22.54	77.5	17.29	82.7	17.29	82.7
Timestream glitches/dropped samples	0.62	76.8	0.13	82.6	0.13	82.6
Intra-MCE synchronization	0.00	76.8	0.06	82.6	0.00	82.6
Inter-MCE synchronization	0.00	76.8	0.04	82.6	0.00	82.6
Frac. of passing channels (MUX col.)	0.10	76.8	0.08	82.6	0.02	82.6
Frac. of passing channels (full expt.)	0.00	76.8	0.07	82.6	0.02	82.6
Raw elnod amplitude not negligible	14.54	62.9	12.45	70.2	13.14	69.6
Elnod stability over scanset	11.56	60.9	9.80	68.7	11.59	66.8
Elnod A/B ratio stability over scanset	16.25	59.3	13.14	67.8	14.03	66.0
Glitches in elnod	2.72	57.8	1.36	66.9	1.55	65.0
Pair-sum elnod model goodness-of-fit	10.65	53.4	6.29	64.5	9.53	62.1
Pair-difference elnod shows structure	6.19	52.7	4.25	64.0	5.61	61.9
TES resistance	2.14	52.1	1.27	63.7	0.94	61.7
Median elnod amplitude	0.40	52.1	0.48	63.7	1.46	61.7
Pair-difference timestream skewness	9.23	51.3	6.54	63.3	8.85	60.4
Change in azimuth-fixed signal during scanset	2.28	51.2	1.91	63.2	2.08	60.4
Excessively high timestream STD	18.57	49.8	14.92	62.4	15.92	59.7
Focal plane-correlated noise	0.00	49.8	0.00	62.4	0.00	59.7
Noise stationarity (per-detector)	5.96	49.2	4.99	61.6	7.10	58.8
Noise stationarity (per-pair)	10.64	49.1	8.00	61.6	10.51	58.7
Mean focal plane temperature	0.00	49.1	0.00	61.6	0.00	58.7
Focal plane temperature stability	0.37	49.0	0.76	61.3	0.27	58.6
Abnormal azimuth scanning	0.02	49.0	0.00	61.3	0.00	58.6
Too many large steps in timestream	0.53	49.0	0.14	61.3	0.38	58.6
Too many destepping attempts	10.04	48.1	7.85	60.2	11.91	56.6
Extreme/variable crosstalk	0.23	47.9	0.16	60.1	0.38	56.3
Frac. of passing halfscans	1.22	47.9	0.49	60.1	1.35	56.3
Frac. of passing data in scanset	9.02	47.4	6.52	59.9	9.59	56.1
Per-pair mapmaking cuts (inc. drop tile 1)	⋯	44.2	⋯	54.4	⋯	51.1

Note. These cuts are applied sequentially in the order listed. The first column (Raw) shows the fraction of data removed by the cut parameter, if no other cuts were considered. For rows after the second, this value is referenced against the total fraction of data from nominally "functional" detectors. The second column shows the fractional remaining data after each sequentially applied round of cuts. Horizontal lines distinguish between (from top to bottom) focal plane yield, cuts applied per-halfscan, cuts applied per-scanset, cuts on cuts, and post-hoc per-pair "channel flag" cuts determined at the mapmaking stage.

each detector's main beam. In the time-reverse sense, the beam partially reflects off one of the flat 50 K filters and travels back through the 4 K optics, refocuses, and reflects again off the focal plane to emerge on sky. This feature has been seen in previous BICEP/*Keck* receivers (Bicep2 Collaboration et al. 2015) and, for most detectors, the integrated power of this ghost beam is <1% of the integrated main beam power. However, tile 1 shows integrated ghost beam power that is 2 −3× larger than that of the other detectors (Figure 27). This anomalous ghost beam power is likely due to the asymmetrical focal plane layout (Figure 9). BICEP3 is equipped with 20 detector modules—slot 21, which is directly opposite to tile 1 on the focal plane, has no module and is covered by a reflective copper plate. Data from all detectors in tile 1 were thus removed from the final analysis in order to pass internal consistency checks.

9. Observing Strategy

9.1. Observing Field

BICEP3 observes the same sky patch as BICEP2/*Keck*, covering $-60° <$ R.A. $< 60°$ and $-70° <$ decl. $< -40°$. However, its

effective sky area is ∼600 deg², larger than the ∼400 deg² in BICEP2/*Keck* due to the larger instantaneous field of view of BICEP3. To avoid regions of high dust contamination in this extended field, we slightly shifted the field center to R.A. = 0 hr, decl. = −55°, compared to R.A. = 0 hr, decl. = −57.5° for BICEP2/*Keck*. About 10% of the observing time is used to map a part of the Galactic plane, centered at R.A. = 15:42 hr, decl. = −53°.

This observing field is known to have very low polarized foregrounds and is covered by other experiments (Figure 28), providing the possibility for joint analyses. For example, we demonstrated in BICEP/*Keck* & SPTpol Collaboration et al. (2021) a method for separating the lensing *B*-mode signal from the potential PGW signature in collaboration with SPT.

9.2. Scan Pattern and Schedule

BICEP3 observes its target CMB sky patch continuously through the austral winter season. At the South Pole, the telescope azimuth and elevation axes conveniently map to R.A. and decl. in equatorial coordinates, respectively. The sky patch

Table 11
Jackknife PTE Values from χ and χ^2 Tests

Band Power	2016 χ 1−5/1−9	2016 χ^2	2017 χ	2017 χ^2	2018 χ	2018 χ^2
Deck jackknife						
EE	0.501/0.383	0.754/0.719	0.982/0.992	0.050/0.108	0.022/0.172	0.122/0.092
BB	0.936/0.998	0.443/0.226	0.731/0.419	0.848/0.563	0.567/0.924	0.130/0.152
EB	0.319/0.283	0.840/0.866	0.263/0.589	0.932/0.838	0.265/0.307	0.832/0.868
Scan dir jackknife						
EE	0.277/0.112	0.956/0.275	0.449/0.453	0.066/0.070	0.198/0.437	0.804/0.459
BB	0.764/0.872	0.525/0.196	0.283/0.433	0.162/0.407	0.168/0.172	0.012/0.030
EB	0.904/0.431	0.697/0.591	0.076/0.228	0.517/0.816	0.838/0.527	0.806/0.798
Temporal split jackknife						
EE	0.998/0.996	0.084/0.257	0.028/0.068	0.277/0.295	0.146/0.467	0.395/0.152
BB	0.098/0.200	0.261/0.255	0.263/0.531	0.331/0.317	0.826/0.946	0.822/0.719
EB	0.958/0.772	0.461/0.713	0.956/0.936	0.020/0.044	0.070/0.034	0.497/0.499
Tile jackknife						
EE	0.257/0.150	0.429/0.623	0.403/0.529	0.559/0.248	0.002/0.004	0.004/0.018
BB	0.527/0.713	0.323/0.495	0.952/0.852	0.455/0.816	0.697/0.862	0.705/0.371
EB	0.707/0.493	0.776/0.872	0.381/0.633	0.517/0.311	0.946/0.984	0.146/0.257
Azimuth jackknife						
EE	0.575/0.866	0.140/0.259	0.776/0.727	0.916/0.962	0.834/0.545	0.695/0.687
BB	0.014/0.126	0.082/0.068	0.178/0.425	0.435/0.667	0.487/0.279	0.860/0.665
EB	0.357/0.415	0.846/0.212	0.487/0.068	0.904/0.363	0.876/0.998	0.164/0.040
MUX col jackknife						
EE	0.309/0.429	0.335/0.363	0.731/0.745	0.232/0.625	0.681/0.946	0.894/0.778
BB	0.665/0.182	0.960/0.423	0.116/0.070	0.840/0.950	0.210/0.657	0.573/0.108
EB	0.451/0.681	0.944/0.992	0.335/0.339	0.423/0.415	0.248/0.353	0.988/0.924
Alt deck jackknife						
EE	0.982/0.996	0.220/0.166	0.972/0.954	0.172/0.405	0.056/0.182	0.102/0.214
BB	0.062/0.635	0.307/0.170	0.251/0.236	0.050/0.100	0.054/0.467	0.152/0.042
EB	0.198/0.192	0.477/0.790	0.411/0.731	0.238/0.118	0.667/0.429	0.513/0.814
MUX row jackknife						
EE	0.776/0.796	0.144/0.068	0.914/0.824	0.345/0.447	0.741/0.359	0.707/0.719
BB	0.822/0.725	0.539/0.631	0.425/0.631	0.561/0.800	0.515/0.673	0.890/0.583
EB	0.850/0.471	0.060/0.166	0.677/0.573	0.383/0.677	0.367/0.601	0.870/0.844
Tile and deck jackknife						
EE	0.631/0.421	0.788/0.878	0.439/0.427	0.888/0.920	0.886/0.926	0.715/0.902
BB	0.902/0.904	0.531/0.477	0.601/0.786	0.441/0.407	0.411/0.567	0.349/0.695
EB	0.311/0.461	0.429/0.569	0.842/0.709	0.204/0.377	0.896/0.944	0.733/0.485
Focal plane inner or outer jackknife						
EE	0.355/0.635	0.822/0.311	0.204/0.224	0.579/0.633	0.174/0.120	0.208/0.327
BB	0.800/0.922	0.711/0.555	0.663/0.928	0.617/0.295	0.148/0.194	0.204/0.283
EB	0.483/0.760	0.303/0.373	0.836/0.974	0.711/0.549	0.132/0.130	0.880/0.635
Tile top or bottom jackknife						
EE	0.942/0.641	0.064/0.010	0.768/0.960	0.505/0.397	0.910/0.679	0.204/0.463
BB	0.974/0.764	0.124/0.012	0.224/0.703	0.046/0.090	0.226/0.705	0.774/0.503
EB	0.353/0.717	0.675/0.593	0.786/0.932	0.411/0.451	0.136/0.345	0.148/0.174
Tile inner or outer jackknife						
EE	0.745/0.665	0.397/0.798	0.828/0.870	0.756/0.930	0.002/0.012	0.014/0.124
BB	0.337/0.667	0.224/0.421	0.196/0.667	0.956/0.818	0.810/0.924	0.076/0.138
EB	0.820/0.900	0.840/0.922	0.216/0.405	0.583/0.756	0.321/0.545	0.321/0.635
Moon jackknife						
EE	0.218/0.709	0.485/0.487	0.860/0.882	0.780/0.878	0.904/0.683	0.104/0.160
BB	0.976/0.824	0.255/0.607	0.996/0.946	0.108/0.246	0.206/0.164	0.142/0.385
EB	0.487/0.900	0.778/0.693	0.088/0.128	0.583/0.463	0.840/0.912	0.701/0.064
A and B offset best and worst jackknife						
EE	0.860/0.794	0.723/0.924	0.571/0.661	0.315/0.537	0.860/0.625	0.908/0.565
BB	0.453/0.561	0.022/0.044	0.970/0.972	0.194/0.293	0.860/0.942	0.814/0.780
EB	0.435/0.455	0.259/0.549	0.806/0.760	0.421/0.285	0.806/0.623	0.776/0.551

then rotates in azimuth but does not move in elevation, allowing us to track it continuously.

The fundamental observing block is a constant-elevation "scanset," consisting of 50 back-and-forth scans in azimuth, at $2.8° \, s^{-1}$ spanning $64.4°$ over 50 minutes. Because the sky drifts by $12.5°$ during each scanset, the azimuth center is shifted every other scanset by $25°$ to track the change in R.A. of the target sky patch (Figure 29). This azimuth-fixed scan pattern allows us to remove ground-fixed pickup and terrestrial magnetic contamination with a simple ground-subtraction template. The elevation is stepped every other scanset by $0.25°$ to fill in coverage between the spatially separated detector beams.

The overall schedule contains cryogenic service and CMB and Galactic plane scansets. These scansets are grouped into "observing phases," and each phase contains between 6 and 10 scansets along with the accompanying calibrations. During a three-day schedule, the telescope completes one cryogenic cycle, six 10 hr phases on the CMB field, one 6 hr phase on the CMB field, and one 6 hr phase on the Galactic plane (Table 9).

The telescope is rotated about its optical axis to a different boresight angle for each schedule. A total of four boresight angles at $23°$, $68°$, $203°$, and $268°$ are used. The pairs of measurements separated by $45°$ are required to measure both the Stokes Q and U parameters. The whole set of four angles is clocked to optimize the coverage symmetry and homogeneity over the target CMB sky patch.

9.3. Detector Calibrations

The detectors in BICEP3 are calibrated in two steps. First, a relative gain calibration is applied to ensure the timestream data from each detector pair accurately subtracts the large common-mode unpolarized signals from the atmosphere, telescope, and CMB. Each scanset is bracketed by an elevation nod (elnod) where the telescope is stepped upward by $0.6°$ then downward by $1.2°$, and finally upward again by $0.6°$ to return to the starting position over the course of one minute. This motion causes all of the detectors to measure varying levels of atmospheric emission according to the relative opacity κ of the atmosphere, described by

$$\kappa = \frac{1}{\sin(\text{el})} \qquad (13)$$

down to elevation el $= 30°$. Each leading and trailing elnod gives a mean gain of detector native feedback units (FBU) per airmass for each channel for the scanset, allowing us to relatively calibrate all of the detectors. A larger "sky dip" spanning $50°–90°$ is performed before each phase as an additional calibration data point for confirming the atmospheric profile.

In addition to the relative gain calibration, the final data set requires an absolute gain calibration. We apply a single scale factor to convert from detector FBU to final CMB temperature units. This scale factor g_{abs} is determined by computing the ratio of the cross spectra of the BICEP3 map with external, calibrated maps from *Planck*. We first calculate

$$g_b = \frac{\langle \tilde{m}_{cal} \times \tilde{m}_{ref} \rangle_b}{\langle \tilde{m}_{real} \times \tilde{m}_{ref} \rangle_b}, \qquad (14)$$

where $\tilde{m}_{real}$ is the uncalibrated BICEP3 temperature map, and $\tilde{m}_{cal}$ and $\tilde{m}_{ref}$ are the *Planck* 95 and 145 GHz maps, respectively. Two
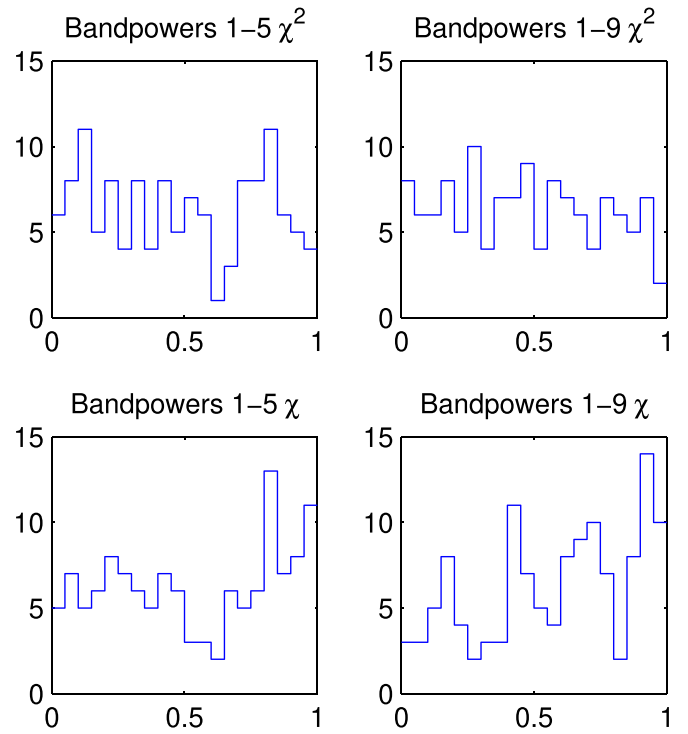

Figure 31. Distributions of the jackknife χ and χ^2 PTE values for BICEP3 2016 to 2018 95 GHz data. They are consistent with a uniform distribution, indicating there is no evidence for systematics at the level of statistical sensitivity.

separate external maps are used to reduce noise. The *Planck* maps are smoothed by BICEP3's beam and reobserved using the same filtering applied to the BICEP3 maps. The ratio of these two spectra is a set of bandpower calibration factors g_b. The final scale factor g_{abs} uses the mean of the first five bandpowers g_b of the BICEP/*Keck* bins.

9.4. Star Pointing

"Star pointing" optical pointing measurements are made with the star camera every few weeks. It has become a routine observation to track the small movements of the telescope mount built on top of snow, though the frequency and quality of star pointings varies depending on the weather. The goal of star pointing observations is to verify the parameters used in the telescope pointing model are stable, including three tilt and two zero-offset parameters along the azimuth and elevation directions, as well as two parameters associated with the offset of the star camera from the mount's boresight rotation axis.

Two separate lists of stars for summer (12 stars) and winter (29 stars) accommodate the change in visibility. The entire set of stars is observed at three distinct deck angles, yielding three sets of independent data points. The sequence involves centering each star, in turn, on the star camera's boresight crosshairs (in practice, one predefined pixel in the CCD), and recording the mount encoders and the current time. This is done for each star at three different boresight rotation angles. The pointing model parameters can be found by fitting the telescope pointing against the star positions. In this process, outliers are dropped and only those schedules with more than 24 data points (in the winter) are kept for data fitting. The rms of the fit residuals typically reaches $\sim 20''$.
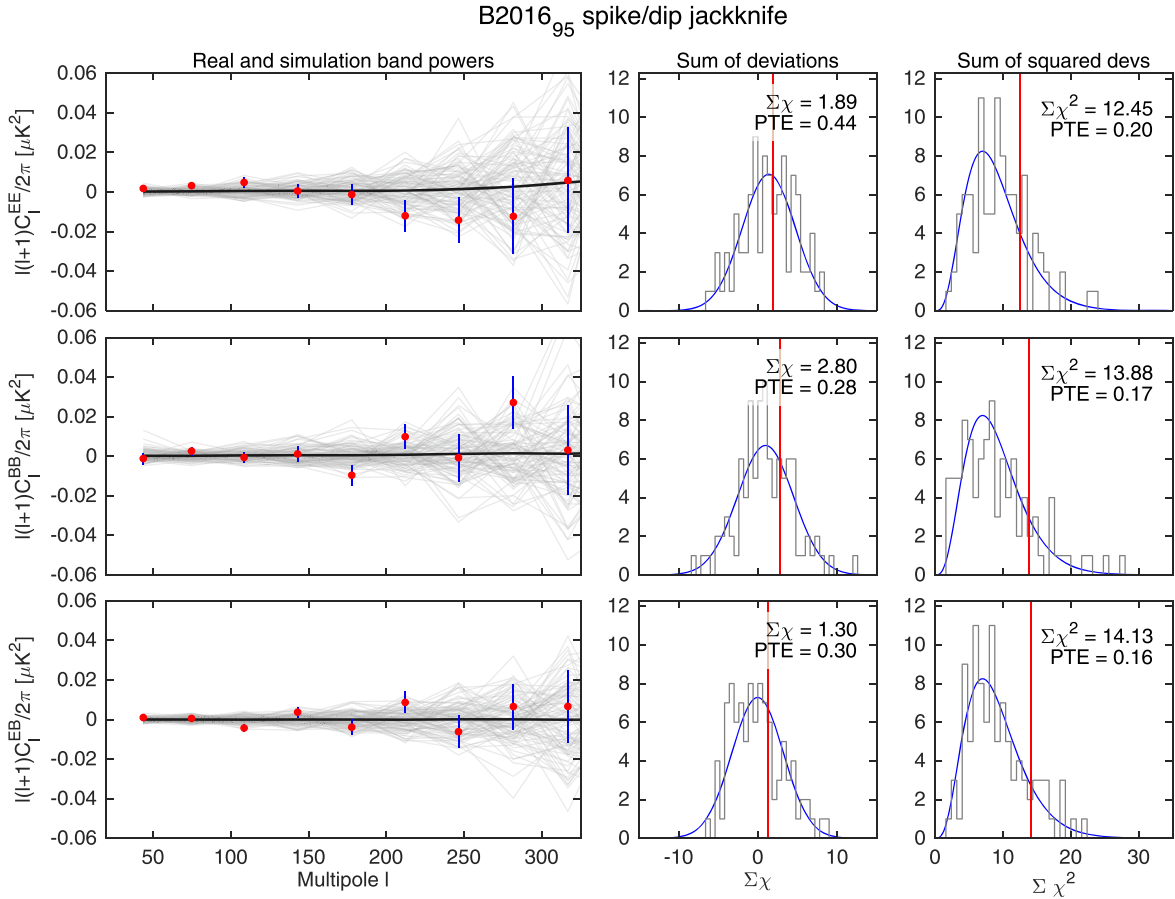
Figure 32. Left: bandpowers for the BICEP3 2016 spike-dip jackknife *EE*, *BB*, and *EB* spectra. The welter of light gray lines are the bandpowers of the ensemble of 99 lensed-ΛCDM + dust + noise simulations, with the mean of these simulations given by the thick black line. The real map bandpowers are given by the red circles, where the error bars are for the standard deviation of the simulations. Right: histograms of the χ and χ^2 statistics for each simulation, with the expected Gaussian and χ^2 distribution overplotted in blue. The real data value is marked by the vertical red line, with the value and corresponding probability to exceed (PTE) annotated.
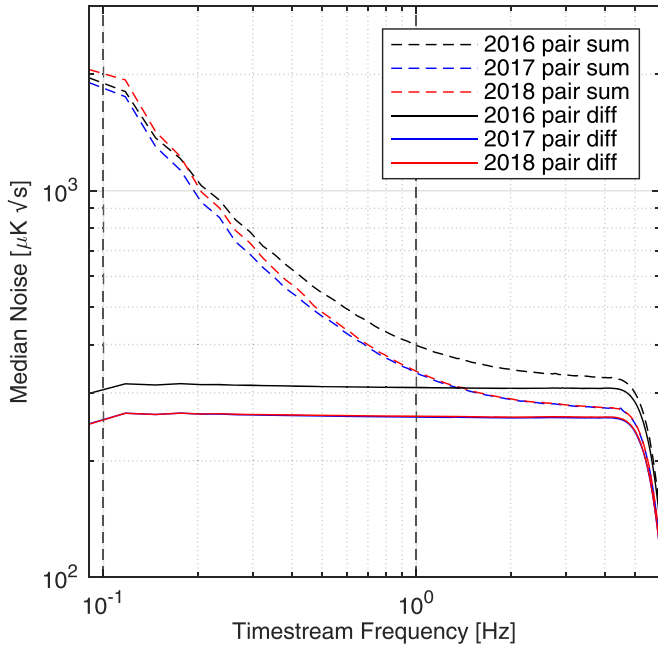
Figure 33. Median pair-sum and pair-diff noise spectra, evaluated from minimally processed timestreams from the BICEP3 2016–2018 seasons. The median per-detector NET is the average within the science band from 0.1–1 Hz.

During the analysis of the 2016 data, we noticed the temporal split jackknife (see discussion in Section 10.3) showed exceptionally low statistical probabilities. It was eventually traced to a shift in the elevation offset parameter derived from star pointings. There was a clear 0.02° shift in this parameter roughly halfway through the season, leading to the jackknife test failures. We associated this shift with a mechanical slip in the star camera mount that was not aligned with the boresight of the telescope, and we added a flexure term in the pointing model for the correction. This flexure term is a step function that has two distinct values over the first and the second half of the season to compensate for the elevation offset shift. In the subsequent investigation, we correlated per-schedule CMB maps against reobserved *Planck* CMB maps. This provided a high temporal resolution boresight tracker to monitor pointing shifts to subarcminute levels, and corroborated our assumption about the pointing shift. This analysis has been incorporated to track anomalous changes in tilting and offset parameters in BICEP and *Keck* telescopes.

10. Three-year Data Set

10.1. Data Selection and Cuts

BICEP3 was installed in the Dark Sector Laboratory (DSL) at the South Pole on 2014 December with a partially filled focal plane. It was populated with a full complement of 20 detector

tiles in 2015 December and began scientifically meaningful observations in early 2016. Grayson et al. (2016) and Hui et al. (2016) show preliminary data quality of BICEP3 during the 2016 season. After the 2016 season, the telescope was removed from the mount and modified during the austral summer. These modifications improved the detector yield, the observation efficiency, and the noise performance, ultimately improving the sensitivity by ∼30% compared to the previous season (Kang et al. 2018).

The detector wafers in BICEP3 were fabricated at the JPL Microdevices Laboratory. A total of 90% of the fabricated wafers achieved ⩾82% in room-temperature impedance screening. The majority of the detector yield losses are associated with wirebond failures in the readout chain. There are more than 22,000 wirebonds in BICEP3, connecting between detector wafers, SQUIDs amplifier chips, and various circuit boards. Failures in critical wirebonds can disable an entire readout column of 22 detectors or an entire row of 30 detectors.

The fully populated focal plane has 1200 optically active dual-polarized detector pairs. At optimal TES bias values, there were 930, 992, and 992 responsive detector pairs in 2016, 2017, and 2018, respectively. Detectors were further down-selected during analysis based on performance in CMB observations and various external calibration measurements. The achieved efficiency in CMB observations and the progression of map sensitivity are shown in Figure 30. Data selection ("cut") parameters and statistics are shown in Table 10. The last round of data down-selection, so-called "channel flags," excludes detectors that are found to be discrepant during mapmaking and external calibration measurements. These may include aberrant beams, absolute calibrations, and the exclusion of the Tile 1 channel discussed in Section 8.10. These detectors are removed for the entire season, and their data are thus excluded from the final coadded maps. The rest of the cut parameters probe a wide variety of data quality metrics at per-detector pair, per-scanset, and per-halfscan levels. Out of all of the responsive detector pairs, BICEP3 achieved overall pass fractions of 57.0%, 65.8%, and 61.8% in 2016, 2017, and 2018, respectively.

10.2. Data Reduction

The data reduction and mapmaking pipeline used in BICEP3 is largely the same as the BICEP2/*Keck* procedure detailed in BICEP2 collaboration et al. (2014b), with only minor modifications to accommodate the larger number of detectors.

10.3. Jackknife Tests

As a standard internal consistency check, we split each year's data set into two halves in various ways. These halves are differenced to cancel out the common signal and leave only noise and the potential contribution of systematic errors. Following previous experiments, we use 14 different jackknives listed in BICEP2 Collaboration et al. (2015) to probe temporal, spatial, and readout systematics.

For a given jackknife j, a vector of bandpowers of $\boldsymbol{d}_j$ is compared to the bandpowers from the ensemble of 499 signal + noise simulations $\boldsymbol{s}_j$ by calculating χ and χ^2 statistics,
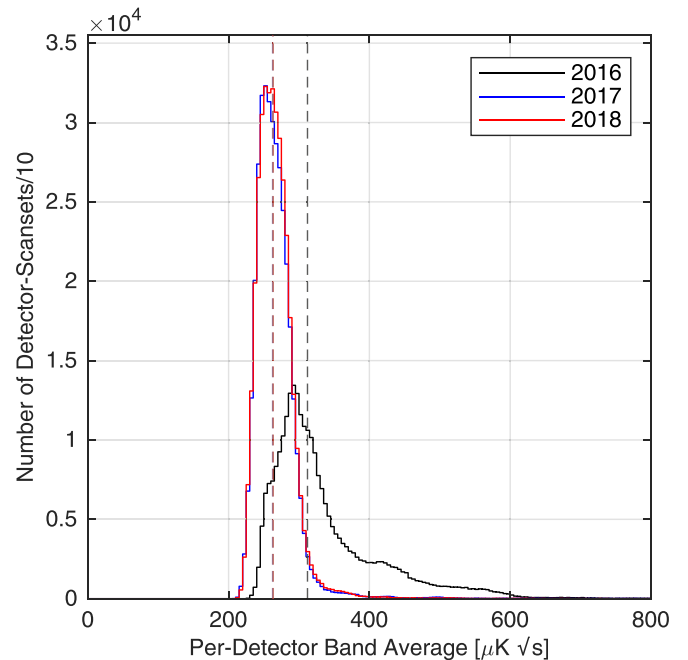

Figure 34. Histogram of per-detector, per-scanset noise for every tenth scanset from 2016 to 2018, after applying a third-order polynomial filter and averaging across the 0.1–1 Hz science band. Median values of $312\,\mu K_{CMB}\sqrt{s}$ and $263\,\mu K_{CMB}\sqrt{s}$ are marked by vertical dashed lines for the 2016 and 2017/18 data, respectively. The reduced internal receiver loading after switching from the metal-mesh infrared filters to the Zotefoam filters, as well as swapping four detector modules, leads to the improved noise performance shown here.

Table 12
BICEP3 Map-based Sensitivity by Season

Season	Map Depth (D)	Eff. Area (A_{eff})	Total Sen. (T)
2016	5.9 μK arcmin	569.2 deg^2	2.9 nK
2017	4.4 μK arcmin	588.1 deg^2	2.2 nK
2018	4.4 μK arcmin	584.7 deg^2	2.1 nK
Total	2.8 μK arcmin	584.9 deg^2	1.3 nK

defined as:

$$\chi = \sum_b \frac{[\boldsymbol{d}_j]_b - \langle \boldsymbol{s}_j \rangle_b}{[\boldsymbol{S}_j]_{bb}}$$
$$\chi_j^2 = (\boldsymbol{d}_j - \langle \boldsymbol{s}_j \rangle)^\top \boldsymbol{S}_j^{-1} (\boldsymbol{d}_j - \langle \boldsymbol{s}_j \rangle) \tag{15}$$

where $\boldsymbol{S}_j = \langle \boldsymbol{s}_j \boldsymbol{s}_j^\top \rangle$ is the bandpower covariance matrix of the corresponding simulations for a single spectral type. The χ and χ^2 values are calculated for real data against the full ensemble, and the real data are judged against the distribution of statistics obtained from the simulations by computing the probability to exceed (PTE).

For the three-year data set, we performed jackknife tests on each year separately, giving a total of 3($EE/BB/EB$) × 14(jack) × 2(χ/χ^2) × 2(bin) × 3(year) = 504 tests. A statistical failure led to the discovery and removal of the tile 1 data discussed in Section 8.10, and the injection of a flexure term to the pointing model discussed in Section 9.4. All of the jackknife tests were then repeated with the updated data set and the final PTE values from the χ and χ^2 statistics are listed in Table 11. Figure 31 shows the distributions of these PTE
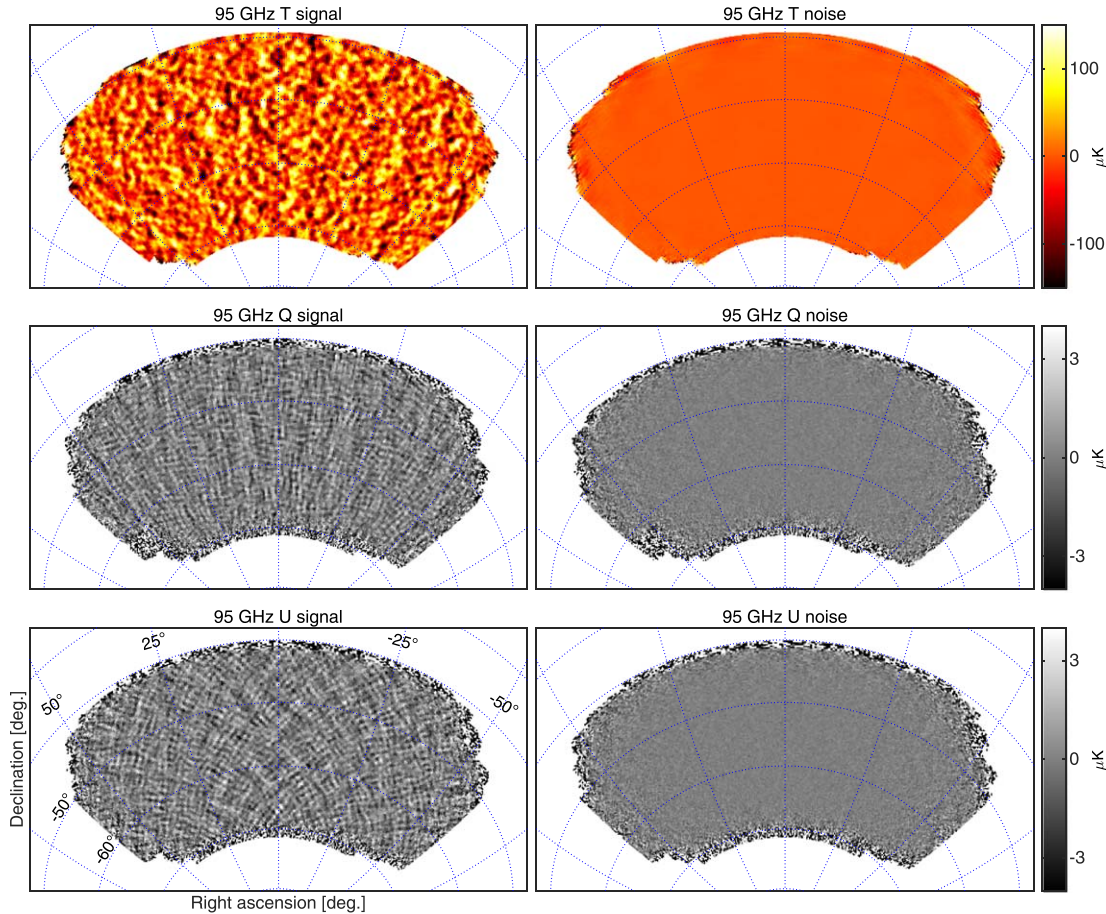
Figure 35. *T*, *Q*, and *U* maps and their jackknifes using the first 3 yr data set from BICEP3. *E*-mode polarization is measured to a high signal-to-noise ratio, evidenced by visually seeing the + and × patterns in the *Q* and *U* maps.

values, which appear to be uniform, showing no evidence of problems at the level of statistical noise.

In addition to the standard 14 jackknife tests, we created an additional spectral jackknife to test the spectral anomaly in the 2016 data due to the metal-mesh low-pass edge filter delamination described in Section 3.6. Using the definition in Equation (4), we selected the worst 50% (the most spikes and dips) of the data, and compared it to the coadded 2017/18 data that have a uniform spectral response. With 99 simulations, we found the difference is consistent with a null result (Figure 32).

10.4. Instantaneous Sensitivity

During normal CMB observation, the detector timestreams are multiplexed, downsampled, and filtered to 30 Hz, which is sufficient for the 0.1–1 Hz science band. The $1/f$ noise, dominated by atmospheric noise, is greatly reduced after pairs of colocated polarization-sensitive detectors are differenced. Contamination from the atmosphere and ground signals is further suppressed by filtering the timestreams with a third-order polynomial and subtracting a ground-averaged template from the scanning data (Figure 33).

The per-detector, per-scanset noise distribution is shown in Figure 34. The median pair-difference, per-detector sensitivity of $312 \, \mu\mathrm{K_{CMB}}\sqrt{s}$ and $263 \, \mu\mathrm{K_{CMB}}\sqrt{s}$ is achieved in 2016 and 2017/18 data, respectively. The sensitivity includes the

weighted combination of every individual detector in every scanset during the three-year observation, capturing both the telescope performance and Antarctic seasonal variation.

We estimate the noise performance of the full BICEP3 instrument by calculating the inverse variance weight used in the final maps, giving the average BICEP3 noise equivalent temperature (NET) as 9.15, 6.82, and $7.14 \, \mu\mathrm{K_{CMB}}\sqrt{s}$ in 2016, 2017, and 2018, respectively, after all cuts are applied.

10.5. Map Depth

The map depth is a measure of the noise level in the polarization maps. Together with the area of the maps, the map depth D, which we define as the deepest, central part of the map (BICEP2 collaboration et al 2014b), sets the final statistical sensitivity of the experiment. This calculation accounts for the nonuniform coverage of the field, weighting each map pixel by its contribution relative to the deepest part of the map. The effective area A_{eff} is calculated using the apodization mask to ensure the maps smoothly fall to zero, thus accounting for the higher variance and lower weight at the edges of the map. The total sensitivity, $T = D/\sqrt{A_{\mathrm{eff}}}$, gives a single number in temperature units indicating the total *B*-mode statistical sensitivity.

Table 12 lists the performance for BICEP3. We achieved a map depth of $2.8 \, \mu\mathrm{K}$ arcmin over an effective area of

584.9 deg^2, for a total sensitivity of T=1.3 nK from the first 3 yr BICEP3 data set. The final T, Q, and U maps and their corresponding noise are shown in Figure 35.

11. Conclusions

We presented the design and performance of BICEP3, which has been observing CMB polarization from the South Pole since 2016. The three-year data set, from 2016 to 2018, reached a map depth of 2.8 μK arcmin (46 nK deg) over an effective area of 584.9 square degrees, corresponding to a total sensitivity of $T = 1.3$ nK. A suite of jackknife tests shows possible sources of systematic false polarization are controlled below the level of statistical sensitivity in each test.

In BICEP/Keck et al. (2021) we present a cosmological analysis using this three-year BICEP3 data set with the combination of data from *Keck*. The combination improves the sensitivity on r to $\sigma(r) = 0.009$. During the austral summers of 2018 and 2019, we observed the CMB cold spot anomaly, which is detailed in Kang et al. (2020). With its achieved sensitivity, BICEP3 can also be utilized for a number of additional science targets, including primordial magnetic fields and axion-like particles through anisotropic and time-variable cosmic birefringence (BICEP2 Collaboration et al. 2017; BICEP/Keck et al. 2021), the properties of interstellar dust grains (Clark & Hensley 2019), and patchy reionization and gravitational lensing through the use of distortion metrics (Yadav et al. 2010).

Additional BICEP3 data taken from 2019 to 2021 are expected to further reduce noise in the 95 GHz power spectrum by a factor greater than $\sqrt{2}$. BICEP ARRAY, which is based on the design of BICEP3, deployed a 30/40 GHz receiver to the South Pole in 2020, which is the first of four planned receivers. In coming years, additional receivers will be deployed at 95, 150, and 220/270 GHz with 32,000+ total detectors (Moncelsi et al. 2020). We project the BICEP/*Keck* experiment to reach $\sigma(r)$ between 0.002 and 0.004 at the end of BICEP ARRAY, depending on foreground complexity and the degree of removal of B-modes due to gravitational lensing (BICEP/Keck & SPTpol Collaboration et al. 2021).

ORCID iDs

C. A. Bischoff ⬤ https://orcid.org/0000-0001-9185-6514
V. Buza ⬤ https://orcid.org/0000-0002-1345-4322
M. Dierickx ⬤ https://orcid.org/0000-0002-3519-8593
M. Halpern ⬤ https://orcid.org/0000-0002-1760-0868
H. Hui ⬤ https://orcid.org/0000-0001-5812-1903
K. S. Karkare ⬤ https://orcid.org/0000-0002-5215-6993
K. Lau ⬤ https://orcid.org/0000-0002-6445-2407
L. Moncelsi ⬤ https://orcid.org/0000-0002-4242-3015
T. Namikawa ⬤ https://orcid.org/0000-0003-3070-9240

References

Ade, P., Bock, J., Bowden, M., et al. 2008, ApJ, 674, 22
Ade, P. A. R., Pisano, G., Tucker, C., & Weaver, S. 2006, Proc. SPIE, 6275, 62750U
Ade, P. A. R., Aikin, R. W., Amiri, M., et al. 2015, ApJ, 812, 176
Ahmed, Z., Grayson, J. A., Thompson, K. L., et al. 2014, JLTP, 176, 835
Albrecht, A., & Steinhardt, P. J. 1982, PhRvL, 48, 1220
Barkats, D., Dierickx, M. I., Kovac, J. M., et al. 2018, Proc. SPIE, 10708, 107082K
Battistelli, E. S., Amiri, M., Burger, B., et al. 2008, JLTP, 151, 908
BICEP2 collaboration, Ade, P. A. R., Aikin, R. W., et al. 2014a, PhRvL, 112, 241101
BICEP2 collaboration, Ade, P. A. R., Aikin, R. W., et al. 2014b, ApJ, 792, 62
BICEP2 Collaboration, Ade, P. A. R., Aikin, R. W., et al. 2015, ApJ, 814, 110
BICEP2 Collaboration, Keck Array Collaboration, Ade, P. A. R., et al. 2017, PhRvD, 96, 102003
BICEP2/Keck and Planck collaborations, Ade, P. A. R., Aghanim, N., et al. 2015, PhRvL, 114, 101301
BICEP/Keck, Ade, P. A. R., Ahmed, Z., et al. 2021, PhRvD, 103, 042002
BICEP/Keck and SPTpol Collaboration, Ade, P. A. R., Ahmed, Z., et al. 2021, PhRvD, 103, 022004
Brout, R., Englert, F., & Gunzig, E. 1978, AnPhy, 115, 78
Buder, I., Ade, P. A. R., Ahmed, Z., et al. 2014, Proc. SPIE, 9153, 915312
Chiang, H. C., Ade, P. A. R., Barkats, D., et al. 2010, ApJ, 711, 1123
Choi, J., Ishitsuka, H., Mima, S., et al. 2013, RScI, 84, 114502
Clark, S. E., & Hensley, B. S. 2019, ApJ, 887, 136
Cornelison, J., Ade, P. A. R., Ahmed, Z., et al. 2020, Proc. SPIE, 11453, 1145327
Crumrine, M., Ade, P. A. R., Ahmed, Z., et al. 2018, Proc. SPIE, 10708, 107082D
Cukierman, A., Ahmed, Z., Henderson, S., et al. 2020, JLTP, 199, 858
Dahal, S., Amiri, M., Appel, J. W., et al. 2020, JLTP, 199, 289
de Korte, P. A. J., Beyer, J., Deiker, S., et al. 2003, RScI, 74, 3807
Gildemeister, J. M., Lee, A. T., & Richards, P. L. 2001, ApOpt, 40, 6229
Grayson, J. 2016, PhD thesis, Stanford University
Grayson, J. A., Ade, P. A. R., Ahmed, Z., et al. 2016, Proc. SPIE, 9914, 99140S
Guth, A. H. 1981, PhRvD, 23, 347
Halpern, M., Gush, H. P., Wishnow, E., & de Cosmo, V. 1986, ApOpt, 25, 565
Henderson, S. W., Allison, R., Austermann, J., et al. 2016, JLTP, 184, 772
Hui, H., Ade, P. A. R., Ahmed, Z., et al. 2016, Proc. SPIE, 9914, 99140T
Hui, H., Ade, P. A. R., Ahmed, Z., et al. 2018, Proc. SPIE, 10708, 1070807
Inoue, A. K., Shimizu, I., Iwata, I., & Tanaka, M. 2014, MNRAS, 442, 1805
Irwin, K., & Hilton, G. 2005, in Cryogenic Particle Detection, ed. C. Enss (Berlin: Springer), 63
Irwin, K. D., Cho, H. M., Doriese, W. B., et al. 2012, JLTP, 167, 588
Kamionkowski, M., Kosowsky, A., & Stebbins, A. 1997, PhRvL, 78, 2058
Kang, J. H., Ade, P. A. R., Ahmed, Z., et al. 2018, Proc. SPIE, 10708, 107082N

Kang, J. H., Ade, P. A. R., Ahmed, Z., et al. 2020, Proc. SPIE, 11453, 114532D

Karkare, K. S., Ade, P. A. R., Ahmed, Z., et al. 2014, Proc. SPIE, 9153, 91533B

Karkare, K. S., Ade, P. A. R., Ahmed, Z., et al. 2016, Proc. SPIE, 9914

Kaufman, J. P., Miller, N. J., Shimon, M., et al. 2014, PhRvD, 89, 062006

Kazanas, D. 1980, ApJL, 241, L59

Kernasovskiy, S., Ade, P. A. R., Aikin, R. W., et al. 2012, Proc. SPIE, 8452, 84521B

Krachmalnicoff, N., Carretti, E., Baccigalupi, C., et al. 2018, A&A, 618, A166

Kuo, C.-L. 2017, ApJ, 848, 64

Leitch, E. M., Kovac, J. M., Pryke, C., et al. 2002, Natur, 420, 763

Linde, A. D. 1982, PhLB, 108, 389

Moncelsi, L., Ade, P. A. R., Ahmed, Z., et al. 2020, Proc. SPIE, 11453, 1145314

Penn, S. J., Alford, N. M., & Button, T. W. 1997, ITAS, 7, 3500

Planck Collaboration, Aghanim, N., Akrami, Y., et al. 2020a, A&A, 641, A1

Planck Collaboration, Akrami, Y., Ashdown, M., et al. 2020b, A&A, 641, A4

Rosen, D., Suzuki, A., Keating, B., et al. 2013, ApOpt, 52, 8102

Seljak, U., & Zaldarriaga, M. 1997, PhRvL, 78, 2054

Sobrin, J. A., Anderson, A. J., Bender, A. N., et al. 2021, ApJS, submitted (arXiv:2106.11202)

Soliman, A., Ade, P. A. R., Ahmed, Z., et al. 2018, Proc. SPIE, 10708, 107082G

Sonka, R., Bock, J. J., Megerian, K. G., et al. 2017, arXiv:1712.05496

Staniszewski, Z., Aikin, R. W., Amiri, M., et al. 2012, JLTP, 167, 827

Starobinsky, A. A. 1980, PhLB, 91, 99

Story, K., Leitch, E., Ade, P., et al. 2012, Proc. SPIE, 8451, 84510T

Takahashi, Y. D., Ade, P. A. R., Barkats, D., et al. 2010, ApJ, 711, 1141

Timusk, T., & Richards, P. L. 1981, ApOpt, 20, 1355

Wiebe, D. V. 2008, PhD thesis, University of Toronto

Willmert, J. 2019, PhD thesis, University of Minnesota

Wong, C. L. 2014, PhD thesis, Harvard University

Yadav, A. P. S., Su, M., & Zaldarriaga, M. 2010, PhRvD, 81, 063512